# THE UNIVERSITY OF HULL

Study of Quantum Dot and Quantum Well Photodetectors

being a Dissertation submitted in partial fulfilment of

the requirements for the Degree of

MSc in Electronic

in the University of Hull

by

Noor Hafidzah Jabarullah, BSc (USM)

SEPTEMBER 2010

# Abstract

A study of quantum dots-in-well infrared photodetectors (QDIPs) yields results useful for the creation of a two-colour QDIP. Quantum dot infrared photodetectors (QDIPs) have been shown to be a key technology in mid and long wavelength infrared detection due to their potential for normal incidence operation and low dark current. This study investigates infrared detectors based on intersubband transitions in a novel InAs/$In_{0.15}$ $Ga_{0.85}$ As/GaAs quantum dots-in-well (DWELL) heterostructure. In the DWELL structure, the InAs quantum dots are placed in an $In_{0.15}$ $Ga_{0.85}$ As well, which in turn is placed in GaAs quantum well with $In_{0.1}Ga_{0.9}As$ barrier. The optical properties of the sample have been studied by the means of photoluminescence and photocurrent using fourier transform infrared spectroscopy. Spectrally tuneable response with bias and long wave IR response at 6.2μm and 7.5μm has been observed.

# Acknowledgement

I would like to thank my supervisor, Professor Stephanie Haywood for her precious time and help. I am extremely glad that she made it possible for me to work in this very interesting project involving new technology of quantum dot detectors. I also express my gratitude to Dr. Sergey Rybchenko for helping me in the experimental work by sharing his knowledge and time. It was a real pleasure to work with him and to learn from such an experienced person. The other person I would like to mention is B. H. Hong and Veronica who also helped me when during the period of my project.

# Contents

# List of Figures

# Chapter 1 Introduction

## 1.1 Motivation of Study

High performance infrared (IR) photodetection is desirable for many applications involving thermal imaging, chemical analysis, night vision, remote sensing, space ranging, mine detection and fibre-optic communications. Depending upon the application, one may desire either different specifications, either a broad, multicolour response from the detector, or a sharp single wavelength response. Multicolour IR detection has the ability to determine the temperature of the observed body, in addition to producing images with some colour depth, so is much more favourable for a general imaging system. Multi-colour focal plane array (FPA) photodetectors are particularly useful for medical and military imaging as well as environmental monitoring applications.

Quantum dots-in-well DWELL are part of a new technology of semiconductor nano-photonic devices, utilising stacked layers of quantum dots (QDs) as the active region in their structures. DWELL photodetectors are a promising new advancement that will hopefully overcome many of the shortcomings of existing IR photodetection systems. QDIPs utilise inter-subband absorption to detect medium and long wavelength infrared radiation within the low absorption, 3-5μm & 8-14μm atmospheric 'windows'. There has been significant research into the study of QDIPs, but little in the way of multi-colour QDIP development, despite their desirability for a wide variety of applications.

The aim of this project is to obtain the optical properties of the sample by photoluminescence and photocurrent measurement while analysing the advantages and disadvantage of quantum-dots-in-well photodetector.

## 1.2 Overview of Dissertation

This project involves on studying the combination or hybrid of quantum-dot and quantum-well, which is known as dot-in-well (DWELL) and optimising the

advantages by this hybrid system the theory of the QDIP. The first part is to understand the background of other photodetectors. The second part is to analyse the optical properties of the samples. Chapter 2 is the review of literature to set out the background information necessary for an understanding of the project results. Chapter 3 details the experimental techniques used in the fabrication and experimental analysis of all the QDIPs samples in this project. The experimental results are presented in Chapter 4. The conclusions from the work undertaken for this dissertation and some recommendations for future work are discussed in Chapter 5.

# Chapter 2 Review of the Literature

## 2.1 Infrared Theory

Infrared refers to the part of the electromagnetic spectrum between the visible and microwave regions (0.75μm to 1000μm). Electromagnetic spectrum refers to the variety collection of radiant energy, from cosmic rays to X-rays to visible light to microwaves, where each of which can be considered as a wave or particle travelling at the speed of light. Infrared radiation can be felt as heat but it cannot be seen with the naked human eye. All objects at room temperature emit radiation mostly concentrated at long-wave infrared. Infrared radiation from the sun is responsible, to a great extent, for heating the earth, the rest being caused by visible light that is absorbed and reradiated at longer wavelengths. Figure 2.1 shows the electromagnetic spectrum. Sir Frederick William Herschel first discovered infrared radiation in 1800 by using a prism to refract sunlight and detecting the radiation through an increase in temperature recorded with a thermometer. Infrared radiation is divided to many sub-bands as shown in Figure 2.2

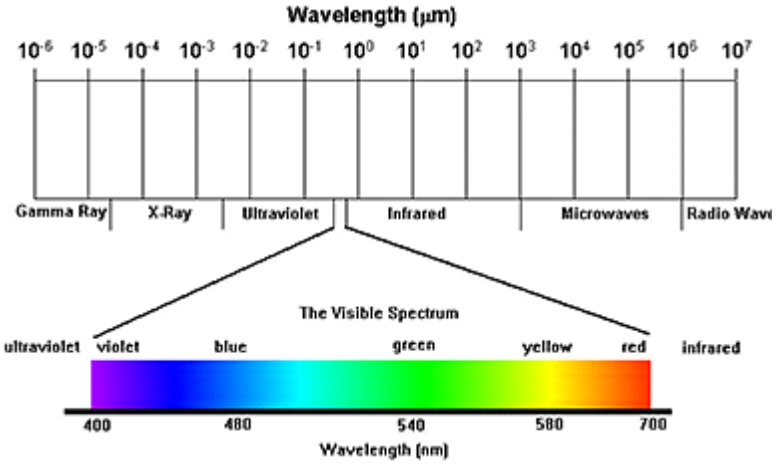


**Figure 2.1: The electromagnetic spectrum – after Colorado, (2010)**

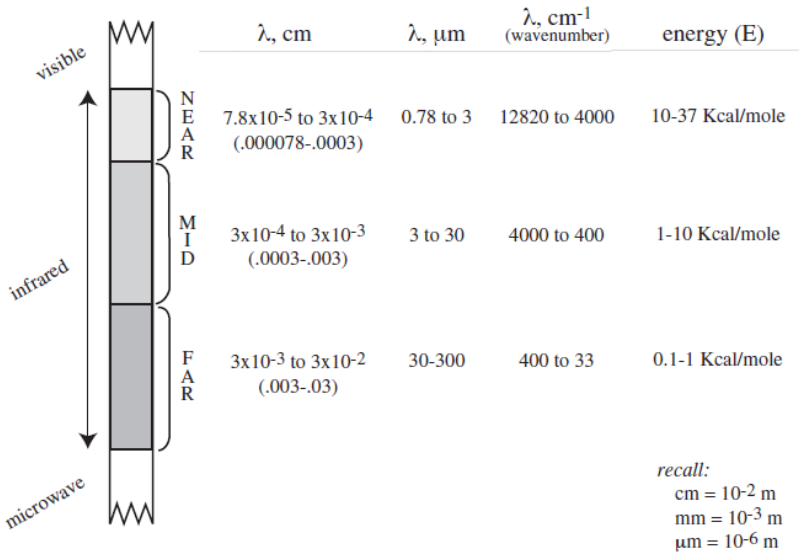


**Figure 2.2 The sub-bands of the IR regions - after Colorado, (2010)**

Infrared detection has applications in many areas of studies and brings together focused areas like optics, solid-state physics, low-noise electronics, cryogenics, statistical analysis, optical communication, astronomy, 2-D imaging, and spectroscopy. Infrared detectors have many applications ranging from military and medical to scientific. The majority of activity for infrared applications has been in military and space applications. The high cost of infrared imaging systems has limited its use in commercial applications. During recent years, infrared detectors have progressed from discrete detectors to large multiplexed 2-D arrays of detector pixels called focal plane arrays (FPA).

## 2.2 Principles of photodetectors

Photodetectors are becoming a standard technology and have been widely used for infrared detection and imaging. Quantum-well intersubband photodetectors QWIPs offer the advantage of being able to manipulate the position of energy levels with respect to the barrier edge in order to minimise the dark current and hence maximise the detectivity and operating temperature for the chosen design wavelength. However QWIPs are not sensitive to light incident normal to the device. This problem can be overcome by further confinement of the electrons in quantum dots to form quantum dot infrared photodetectors

(QDIPs). These use optical transitions between bound states in the conduction/valence band of the quantum dots. Further potential advantages of QDIPs are a low dark current and relatively temperature independent performance. Combining the quantum dot and quantum well systems can result in devices with the advantages of both systems plus voltage tenability. This literature will cover the background of basic photodetectors, moving to Quantum Wells (QWs), then Quantum Dots (QDs) and finally the hybrid of both QWs and QDs which is Dot-in Well (DWELL).

Photodetectors are semiconductor device that can detect optical signals through the electronic processes. The photodetector detects the luminescent power falling upon it and converts the variation of this optical power into a correspondingly varying electric current. Several different detectors that existed are photomultipliers, pyroelectric, semiconductors based photoconductors, phototransisitors, and photodiodes. They are normally divided into two groups; photon detectors and thermal detectors. The photon detectors are based on the quantum photoelectric effect where a photon excites an electron-hole pair which converted to the photocurrent. The other one which is the thermal detectors detect light by sensing the temperature increase when the light energy is absorbed at their dark surface. They are more like thermal sensors and suitable for far-infrared wavelengths. The general operation of photodetectors involved a few simple steps, carrier generation by incident light, then carrier being transported or multiplication by current gain mechanism in case of the presence and finally the interaction of current with the external circuit to give the output signal. Photodetectors have a wide range of use, including infrared sensors in optoisolators and optical fibre communication detectors. Therefore photodetectors must meet the strict requirements such as high response speed, minimum noise and high sensitivity at operating wavelength. In addition ideal photodetectors should also be small and compact, reliable during operating conditions and use low biasing voltage and current (Parker, 1994). A basic concept of photodetector using p-n junction example fabricated using silicon is shown in Figure 2.3.

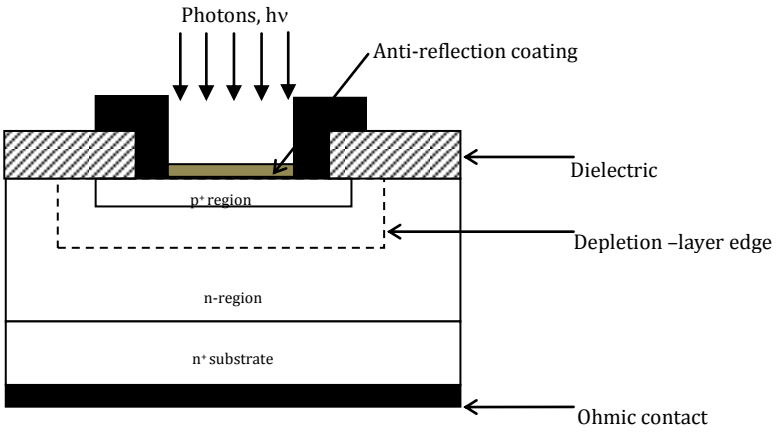


**Figure 2.3: A basic photodetector concept using p-n junction.**

Photons are the incident on top of the diode surface. If the photons have enough energy to enter the device to generate electron-hole pair, an anti-reflection coating is often applied to reduce the reflection of photons from the device surface. The coating can be single or multiple layer dielectrics with the thickness layer of the dielectric to minimize reflection at the suitable wavelength. The photons will then be able to create electron-hole pairs if their energy is bigger than the semiconductor band gap. Thus the photoelectric effect is based on the photon energy $h\nu$, the incident photon wavelength is related to energy transition ΔE in the device which the below relationship;

$$\Delta E\ (eV) = \frac{hc}{\lambda} = \frac{1.24}{\lambda} \tag{2.1}$$

Where λ is the wavelength (in microns), c is the speed of light and ΔE is the in most cases is the energy or band gap of the semiconductor (Wilson & Hawkes, 1998).

The measure of performance for general capacitor can be measured in three parameters; the quantum efficiency and gain, the responsivity and the detectivity. Quantum efficiency η, is the number of electron-hole pairs generated per incident photon.

$$\eta = \frac{I_{ph}}{q\Phi} = \frac{I_{ph}}{q}\left(\frac{h\nu}{P_{opt}}\right) \tag{2.2}$$

where $I_{ph}$ is the photocurrent, $\Phi$ is the photon flux, and $P_{opt}$ the optical power. The ideal quantum efficiency is unity, where the reduction usually comes from current loss due to recombination, incomplete absorption and reflection. Response speed is usually limited by three factors: diffusion carriers, drift time in the depletion region and the capacitance in depletion region. Responsitivity R, is one of the parameter to measure the photodetector sensitivity.

$$R = \frac{I_{ph}}{P_{opt}} = \frac{\eta q}{h\nu} = \frac{\eta \lambda}{1.24} \text{ Amps/watt} \tag{2.3}$$

To further improve the signal some photodetectors have internal gain mechanism, which unfortunately leads to higher noise. Low noise is pivotal for the minimum detectable signal strength. This is where the SNR (signal-to- noise ratio) is involved. One factor that can contribute to noise is the dark current that caused leakage current when the photodetector is in biased but not exposed to light source. Another cause of noise is the device temperature during operation that must be smaller than the photon energy. Other source of noise could be from background radiation such as black-body from the detector housing if it is not cooled down. Internal noise such as thermal noise in the device also contributes to the device temperature. The noise due to random effects associated with surface traps and generally has 1/f (flicker noise) characteristics. The generation and combination event also contributes to the noise factor. In a nutshell all noise are independent events and can come from optical and thermal processes. All these noises can be added together as a total noise called the noise-equivalent power (NEP). The photodetectors detectivity therefore can be defined as D*(Dee-star);

$$D^* = \frac{\sqrt{AB}}{NEP}\ cm - Hz^{1/2}/W \tag{2.4}$$

where A is the area and B is the bandwidth. This is also SNR when 1Watt of light incident power on a $1cm^2$ of a detector measured over a 1-Hz bandwidth, and then normalized to the area since the noise is generally proportional to the square root of area. Generally the detectivity depends on the sensitivity of

detector, spectral response, and noise which is in a function of wavelength, modulation frequency and bandwidth.

What makes the photodetector a good one is the photon detection which lies in the depletion region. To absorb as much of the incoming photons as possible the depletion region has to be made very wide. A wide depletion region also means a smaller junction capacitance, and good quantum efficiency, but increased transmit time for carriers to cross the depletion region. The parameters such as photon wavelength and material detection are usually fixed, so the only left to tailor is the depletion region width. The best way to define the depletion region in the photodetector is by using the p-i-n photodetector (Sze & Ng, 2007). The p-i-n photodiodes is one of the common photodetectors due to the intrinsic layer can be tailored to optimize the quantum efficiency and the frequency response.

## 2.2 Quantum well and quantum dot photodetectors

Quantum well structures are considered as very promising systems for infrared photodetectors. Traditional interband optical absorption involving photogenerated carriers across the band gap $E_g$ which promotes electron from the valence band to the conduction band excited state are shown in Figure 2.4. In the photodetector structure the photocarriers are collected therefore producing photocurrent. Certain application requires long wavelength infrared detection which needs small band gap material. These materials are usually complex and expensive to grow, process and fabricate compared to large band gap materials. Conventional material used in the mid-wavelength infrared (MWIR) and long-wavelength infrared (LWIR) are mainly HgCdTe (HCT). According to Rogalski (2003), HCT are difficult to systhesize and soft thus suffers from non-uniformity making the fabrication very expensive. Therefore different QWIP made of AlGaAs/GaAs, InGaAs/InP, Si/SiGe, InGaAs/GaAs and other heterostructure have been used, and achieved good commercial success. GaAs based materials have been the main interest due to its good growth structure and does not suffer from material uniformity problems like HCT (Haywood, et al., 2006). The imaging performance of focal plane arrays

fabricated with this base material are comparable to the state-of-the-art of HCT detectors (Martyniuk, et al., 2008).

For large band gap materials it is much more efficient to use intersubband transition (IBST) that perform transitions between energy levels within the same valence or conduction bands. Quantum wells are used to create the state of transition within valence or conduction bands.

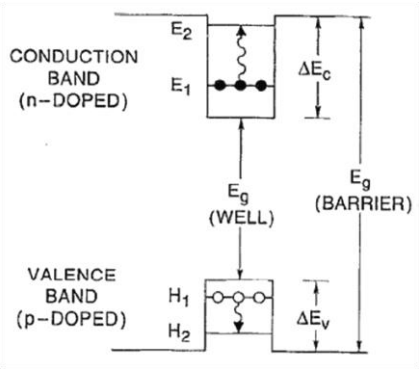


**Figure 2.4: Band gap structure of quantum well and intersubband transitions between $H_1 \rightarrow H_2$ and $E_2 \rightarrow E_1$ – source from Levine (1993).**

The first functional quantum well infrared photodectectors (QWIPs) was reported in 1987. The QWIPs was based on bound-to-bound intersubband transitions in GaAs/AlGaAs heterostucture and later improved to bound-to-continuum transition in 1988. In 1991 bound-to-miniband transition had also been observed (Rhyzii, 1997). These quantum well intersbubband photodetectors (QWIP) offer better flexibility compared to interband transitions and the operating wavelengths can be tailored using different quantum well widths or combination of well and barrier materials (Gupta, et al., 1999). However QWIP has a few disadvantages and one of them is lack of normal incidence absorption due to polarization selection rules. This requires additional processing usually employed $45^o$ edge facet geometry can be seen as shown in Figure 2.5.

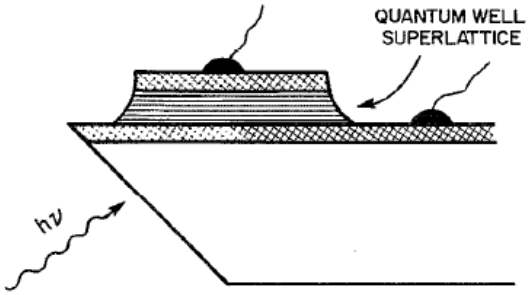


**Figure 2.5: Light incident is normal to a polished facet making 45° angle to the quantum well – source after Schneider & Liu (2007).**

The other problem is low internal quantum efficiency due to small number of carriers in the transitions compared to interband detectors. Efficiency can be enhanced by increasing doping but this will lead to high Fermi energy level thus will directly raise the noise level for the given operating temperature. Another main factor that bounded the quantum well intersubband transition is its thermionic transmission over the barrier (Gupta, et al., 2004). Generally it can be reduced by lowering or cooling the detector's temperature but will make the QWIPs more expensive to fabricate, bulky therefore inconvenient to use. As a solution to this degradation and limitations is the quantum dot infrared photodetector (QDIP). QDIP are similar to QWIP but with the quantum wells replaced by the quantum dots arrays which plays important role for a photosensitive base and have size confinement in all spatial directions as shown in Figure 2.6. QDIP have been demonstrated by a few groups where the self-assembled dots are fabricated using the Stranski-Krastanow growth mode during molecular beam epitaxy (Philips, 2002).

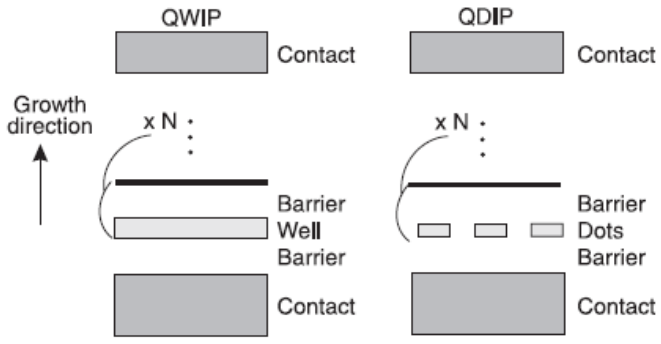


**Figure 2.6: The schematic layer of QWIP and QDIP neglecting the wetting layers –source from Liu (2003).**

Comparing to QWIPs, quantum dot photodetectors have advantages such as multi-wavelength detection. This new intersubband photodetector can significantly surpass QWIPs as it is very sensitive to normal incidence contrast to QWIP where the limitation is due to the absorption selection rules (Mashade, et al., 2003). Another major advantage of QDIP is the low dark currents due to three dimensional quantum confinement which enable higher operating temperatures. QDIP also has the advantage of its long electron lifetime which has been anticipated to lead slow intersubband relaxation time due to phonon bottleneck (when the inter-level spacing is larger than the phonon energy). Longer electron lifetime therefore leads to higher responsivity, and higher operating temperatures.

In real application it is a challenge to meet all the anticipations of QDIPs. The main disadvantage of QDIP is the inhomogenous linewidth of the quantum dot group variation of dot size in the Stranski-Krastanow growth mode directly reduced the absorption coefficient. Quantum dots also have many parameters for tuning the energy spacing between the energy level such as the quantum dot shape, size, material composition and strain which is very challenging for wavelength tuning.

Improvements to the QWIP performance have been shown by replacing the quantum wells with quantum dots or quantum wire. Multicolour QWIPs also has been proposed. However these improvements have their own disadvantages and equalised the drawbacks of the conventional QWIPs (Ling, et al., 2008; Rogalski, 2002). The most recent interest is in developing intersubband quantum dot detectors in the MWIR and LWIR due to the potential of low dark current with normal incidence operation. However quantum dots do not have specific parameters in obtaining a desired spectral response from the detectors. Thus combining the QWIP and QDIP advantages can control the quantum dot parameters by engineering the quantum well sizes. This device is called quantum dot-in-well (DWELL) heterostuctures where the quantum dots are embedded in a strain-relieving quantum well. For example of this device are the

InAs dots placed in the InGaAs well, which represent hybrid of traditional QWIP with the recent QDIP(see Figure 2.7).

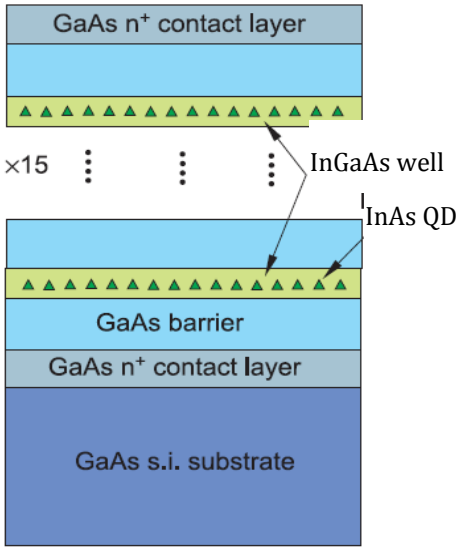


**Figure 2.7: Example of DWELL infrared detector device structure - source from Rogalski (2009).**

This device has a potential of voltage tunability, multicolour operation, good control over the operating wavelength and higher operating temperatures especially in very long wavelength IR response. The biggest challenge for this detector is low responsivity and quantum efficiency which could be improved by adding more dot-in well layers (Krishna, 2005). Generally these detectors have the potential to be a new technology with high operating temperature and wide range of operation from mid wavelength IR to very long wavelength IR.

This study will be comparing the achievements of QWIPs and QDIPs technologies and combines the unique systems to a hybrid system called DWELL photodetectors. Parallel with the third generation photodetectors system that are being developed nowadays, these systems can provide capabilities like better frame rates, enhanced thermal resolution as well as multicolour functionality. These quantum dots and DWELL photodetectors are still in the early stage of development and many improvements can be made for commercial use. Ideal detector systems for the future application will require in depth on the device structure, material properties, and their impact on all

spectral regions. QDIPs and DWELL system is an open area which needs to be optimized and can be exploited for smart sensors use to improve current photodetectors technology.

# Chapter 3 Description of Method and Procedures

## 3.1 Introduction

This research is focused on experimental works on two QDIPs samples. The details of the experimental background and methodology are outlined in this chapter. The brief description of the sample growth structure and device fabrication will first be presented. Experimental studies are concerning of the optical characterisation of two QDIP samples. Photoluminescence setup and procedures will be explained by utilising FTIR spectroscopy. Photocurrent experimental procedures will also be demonstrated towards the end of this chapter.

## 3.2 Sample Growth Technique

***Molecular Beam Epitaxy***

Molecular Beam Epitaxy (MBE) is a technique for epitaxial growth invented by Alfred Y. Cho and John Arthur around the 1960s in the Bell Labs. MBE has moved quantum research from theoretical to practical realm by introducing the technique of growing thin layers of semiconductor material which can contain three to four elements in one time (A.Y.Cho, 1971). This technique occurs on a surface of heated crystalline via the interactions of one or several molecular/atomic beams. In late 1980s, MBE was challenged by Metal Organic Vapour Deposition (MOVPE) as the most efficient and best technique for this purpose. However, MBE is still very much attractive for its affordable method of high quality crystal growth for many semiconductor materials, such as SiGe, GaAs and grapheme and its versatility. In figure 3.1 is the illustration of typical MBE growth system where the growth process operates in an Ultra High Vacuum (UHV). UHV at very low background pressure around $10^{-10}$ - $10^{-11}$ Torr, is an important environment for MBE.

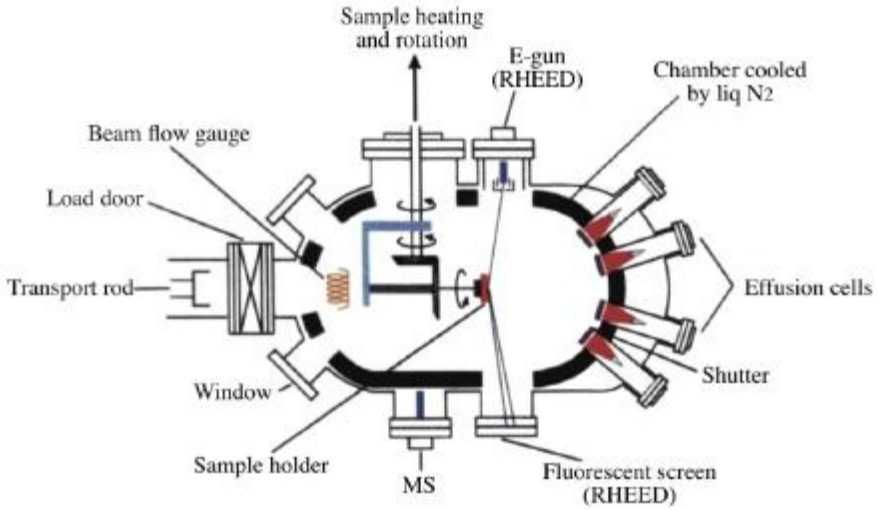


**Figure 3.1: A schematic diagram of MBE system for the growth of III-IV compounds- source from Chang .et al., (1973).**

The Knudsen cells (K-cells) are to provide angular distribution of atoms or molecules in a beam (Figure 3.2). The solid materials such as Galium, Indium, Arsenic or Aluminium are placed in the effusion cells and vaporised towards the substrate. The substrate is heated to the necessary temperature and continuously rotated for improving the growth homogeneity.

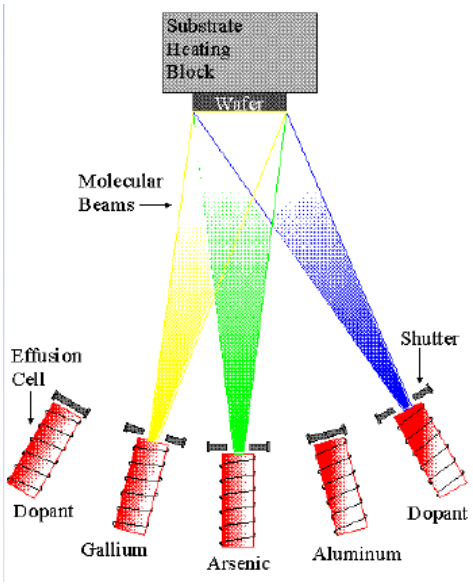


**Figure 3.2 Schematic of the growth chamber – source from A.Y.Cho (1979)**

Usually the crubicles chosen is pyrolitic boron nitride (PBN) to ensure the material in the chamber has to be as low as possible and chemical stability up to

1400ºC. Only pure materials like molybdenum and tantalum are mainly used for the shutter heaters and other components. The reach UHV a bakeout of the whole chamber for 24hours is required at approximately 200ºC. This UHV in the growth chamber keeps the background contamination low and also ideal for many in-situ characterisation tools such as reflection high energy electron diffraction (RHEED) and also allows Auger techniques to be used. The RHEED oscillation signal corresponds exactly to the time needed to grow a monolayer (ML) and the diffraction pattern on the RHEED windows gives direct indication over the stage of growth on the surface as shown in Figure 3.3

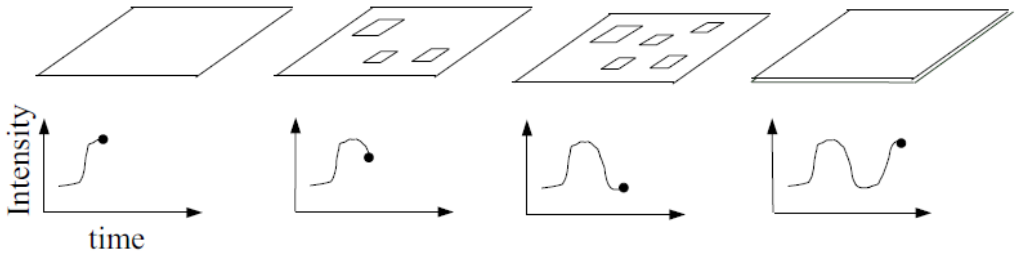


**Figure 3.3 Extracting information on growth from RHEED image intensity – source from Rinaldi (2002).**

The cryogenic screening around the substrate can help to minimise the spurious fluxes of atoms and molecules from the chamber's wall. MBE systems allow control of the chemical composition and doping level by opening and closing of the mechanical shutters. The operation time of a shutter is usually very fast (about 0.1 seconds), than the time of one ML which is typically 1-5 seconds. Careful control of the temperature of the effusion cells via PID controllers permits the control of intensity of the flux for each component or dopant very accurately (better than 1%). The growth rate of MBE is typically about 1μm/hour and capable of growing very thin layers and produce very high quality results.

## 3.3 Sample Growth and Structural Characterisation

The samples used in this study are grown in a VG Semicon V-80 molecular beam epitaxy (Figure 3.4) in the ESPRC National Centre for III-IV semiconductor Technology by the University of Sheffield group.

**Figure 3.4 The MBE Facility VG- V80 used to grow the samples in The University of Sheffield.**

The InAs/$In_{0.15}Ga_{0.8}As$/GaAs dots-in-well (DWELL) structure is grown on a GaAs semi-insulating substrate with 30 periods of the DWELL. These active regions of 30 layers are separated by 500Å thick of $Al_{0.1}Ga_{0.9}As$ barriers. The DWELL layers consist of 2.4MLs of InAs in a 20Å of $In_{0.15}Ga_{0.8}As$ quantum well (QW) which in turn is surrounded by GaAs QW.

First, is the oxide desorption from the semi-insulating GaAs substrate, at 650ºC for ten minutes. Then, the equivalent thermocouple temperatures for various required temperatures for the growth of different layers are measured. After the appropriate measurement had been made, a 300Å of AlAs which acts as etch-stop layer is grown to allow for substrate removal during fabrication process of focal plane array (FPA). Applications of the etchants are suitable for fabrication of variety of novel high-performance heterostructure devices (Broekart & Fonstad, 1992). On top of the etch-stop layer, a 5000Å $n^+$GaAs bottom contact layer doped with Silicon at a doping concentration of 2x $10^{18}/cm^3$ is grown at 590ºC. After that a 500Å thick of $Al_{0.1}Ga_{0.9}As$ barrier is grown at the same temperature. Then, after the barrier is grown, a 300 seconds growth interrupt is

started to reduce the substrate temperature from 590°C to 470°C for the DWELL layers to be grown. After the interrupt, a 10Å of GaAs is grown followed by a 20Å (for the second sample this layer is doped with silicon doping concentration of 2.5-3.0x$10^{-10}$$cm^{-2}$ or approximately 1 electron/dot. The layer is then continue to be topped with another 10Å of GaAs, contributing to the total 0f 40Å thick of GaAs. After the GaAs QW a InAS quantum dot is grown. Indium has a low sticking coefficient and floats on the surface, therefore 0.716 MLs of InAs is introduced to prevent compositional gradient for the $In_{0.15}Ga_{0.8}As$. The thickness of this InAS pre-adsorbed layer varies depending on the thickness of GW and growth temperature. After that, InAs floating layer is put down on the substrate by a 10Å thick $In_{0.15}Ga_{0.8}As$ layer which is the first layer of the $In_{0.15}Ga_{0.8}As$ is grown. It has been discussed in literatures that InAs QD grown on an $In_{0.15}Ga_{0.8}As$ layer has higher density compared to QDs grown on GaAs. Immediately after the growth of $In_{0.15}Ga_{0.8}As$ layer, a 1.083MLs of InAs wetting layer is grown followed by additional of 0.6MLs is deposited which formed the quantum dots. The density of the InAs QDs is found to be 2.5-3x$10^{10}$ $cm^{-2}$ from the atomic force microscopy (AFM). The AFM image of the 2.4MLs InAs on a 10Å $In_{0.15}Ga_{0.8}As$ QW is shown in Figure 3.5

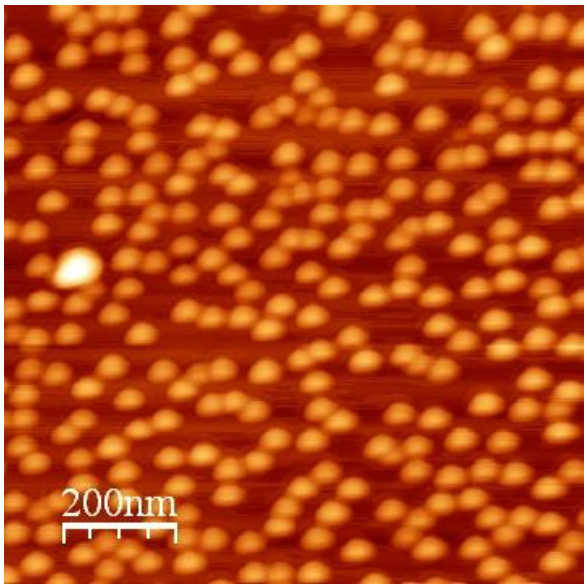


**Figure 3.5 The AFM image of 2.4MLs of InAs on a $In_{0.15}Ga_{0.8}As$ QW**

Following the growth of the InAs, in a 10Å thick of $In_{0.15}Ga_{0.8}As$ QW. After that, a 68.5Å thick of GaAs QW is grown. The growth rates used for In, Ga and Al are 0.519ML/sec, 0.9ML/sec and 0.1ML/sec respectively. Then, after the growth of GaAs, a 180 seconds of growth interrupt with As shutter opened is placed to ramp the temperature from 470°C to 590°C for the $Al_{0.1}Ga_{0.9}As$ barrier to be grown. Finally a 5000Å thick $n^+$ GaAs top contact layer is grown at the same temperature as the barrier. The GaAs contact layer is directly doped with Silicon at a doping concentration of 2x $10^{18}/cm^3$. The device structures are shown in Table 3.1.

| Sample | VN1485 | VN1486 |
|---|---|---|
| Top contact | 500nm GaAs; n= $2x10^{18}cm^{-3}$ | |
| 5nm $Al_{0.1}Ga_{0.9}As$ (x30) | Undoped | |
| 6.85nm GaAs (x30) | Undoped | |
| 1nm $In_{0.15}Ga_{0.85}As$ (x30) | Undoped | |
| 2.4ML InAs QD (x30) | Undoped | |
| 1nm $In_{0.15}Ga_{0.85}As$ (x30) | Undoped | |
| 1nm GaAs | Undoped | |
| 2nm GaAs | Undoped | n=2.5-3 x $10^{10}cm^{-3}$ /1 electron per dot |
| 5nm $Al_{0.1}Ga_{0.9}As$ | Undoped | |
| Bottom contact | 500nm GaAs; n= $2x10^{18}cm^{-3}$ | |
| Etch-stop layer | 3nm AlAs | |
| Substrate | Semi-insulating GaAs | |

**Table 3.1: The device structure of samples VN1485 and VN1486**

## 3.4 Device fabrication

Device fabrication is done in a class-100 clean room in University of Sheffield where the 400μm x 400μm mesas were defined using photolithography, followed by metal evaporation and then etching techniques. The first stage was to define the mesa structure for the QDIPs using standard photolithography following steps were carried out for each sample:

1. The sample is cleaned using trichloroethylene (TCE), ultrasonic bath cleaning with acetone and ethanol, and with a final rinse in distilled/deionised water.
2. Then the sample is heated in an oven at 85°C for 5 minutes in order remove residual solvent.
3. Spin coat of the photoresist (AZ5214 resist) at a speed of 4000rpm for 30s.
4. The sample is then soft baked in an oven at 90°C for 15 minutes.
5. The most critical process is the photolithography was done by masking of the sample and exposed to focussed light from a mercury vapour lamp for 25s.
6. Development of the sample in a solution with a 2:1 ratio of developer to $H_2O$ for 20s. This process left a pattern of two rows of photoresist squares on the sample in order to make multiple QDIPs on each sample (Figure 3.6(a)).
7. The patterned sample is hard baked in an oven for 2 minutes at 120°C to cure the photoresist in preparation for etching.
8. After that is the chemical etching process to scrape away the unmasked area of the sample down to the depth of the Si-doped GaAs bottom contact layer, defining the mesa structures.
9. Finally is the removal of the photoresist using acetone.

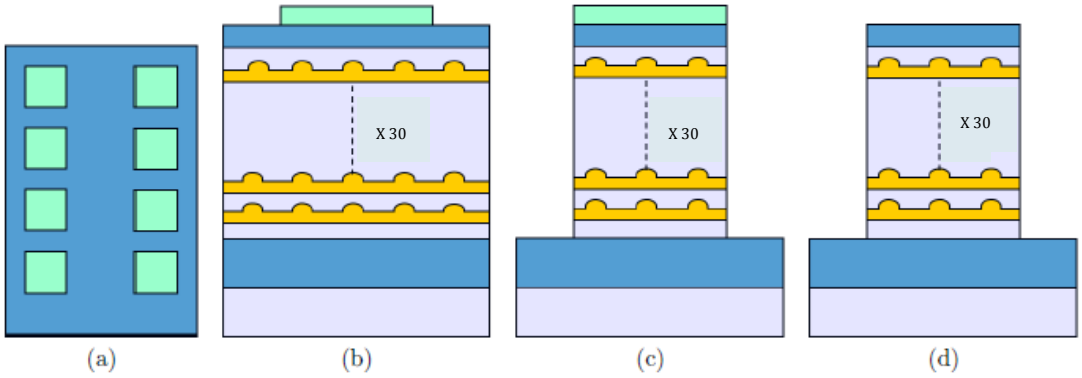


**Figure 3.6: The schematic of the mesa structure processes. (a) The top view of the patterned sample, with the photoresist marked in light blue. (b) The sample cross-section with the photoresist square on top. (c) Cross-section etching process. (d) A single mesa cross-section after photoresist been removed - reproduced from Sze & Ng( 2007).**

The second stage was the formation of the metal contacts and the final packaging. Another photolithography step was carried out to define areas for the metal contacts on the QDIPs. The lithography procedure described in the steps above was repeated using a different mask for the metal contacts. The pattern for the contacts consisted of leaving clear circles of 200μm diameter on top of each mesa and long clear rails on the bottom contact layer, with the rest of the sample covered in photoresist. This will allow each QDIP on the sample would have an independent top contact and a shared bottom contact. After the second photolithography step, metal contacts were formed first removing of natural oxidation by cleaning the sample in HCl (10%) for 40s. The using evaporation method, layers of Ge, Ni and Au been deposited for the n-type metal contacts. After that is the lift off process by using acetone to remove the photoresist from the sample. The final step consists of annealing the contacts using rapid thermal annealing under $N_2$ flow at 400°C for 45 seconds

The device was finally packaged by mounting it on a 12-pin TO5 header, as shown in Figure 3.7, with 25μm thick gold wires were bonded to the metal contacts on all the QDIPs in the sample, connecting them to the gold pins on the header. This step is important in order to characterise the sample using photocurrent measurement.

**Figure 3.7: 12-pins TO-5 Header**

Below are the processes of the wire bonding using the manual wire bonder Kulicke & Soffa (Figure 3.8):

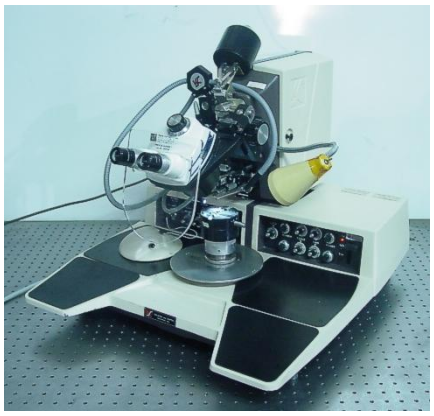

**Figure 3.8: Kulicke & Soffa Manual Wire Bonder.**

1. The sample needs to be cut into the size that fits the TO-5 header. Figure Using the microscope (x400) to see the mesa structure, the sample is scratched using diamond scriber and then broken easily using slight pressure at the end of the line.
2. The sample is then cleaned using alcohol.
3. The sample is attached onto the TO-5 header surface using gold epoxy (able bond 8370).
4. Next, the sample is cured in the oven at 180º C for one hour to enhance the bonding.
5. After curing the sample is ready to be bonded using the wire bonder. The work holder plate is heated up to 100ºC while bonding the gold wire

onto the sample (Figure 3.8). The ready bonded sample is shown in Figure 3.10 using top view.

**Figure 3.9: The work holder plate of the manual wire bonder.**

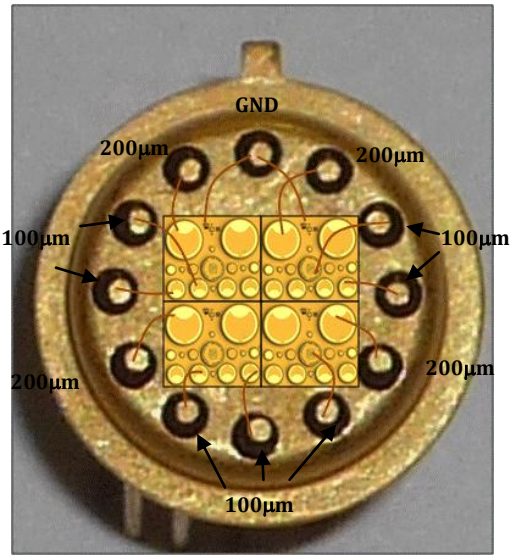


**Figure 3.10: The top-view of the ready bonded sample with gold wires and the details of the device contact.**

## 3.4 Energy Band Structure

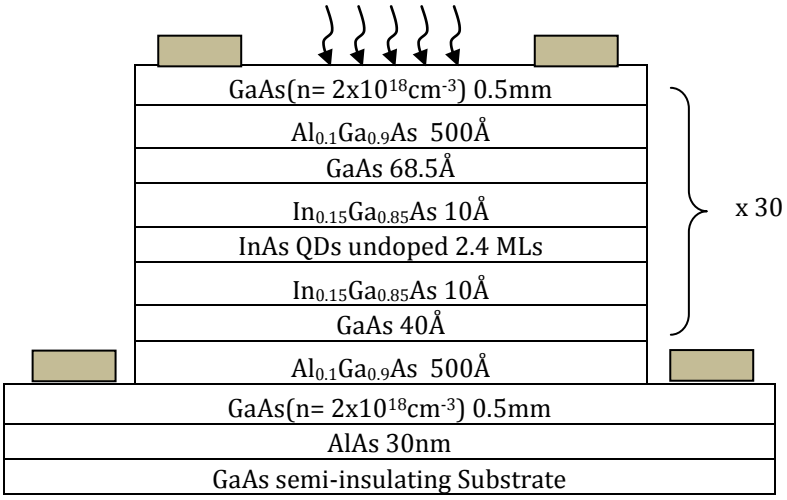


**Figure 3.11: Heterostructure of schematic of InAs/ $In_{0.15}Ga_{0.8}As$/GaAs dots-in-well infrared photodetector.**

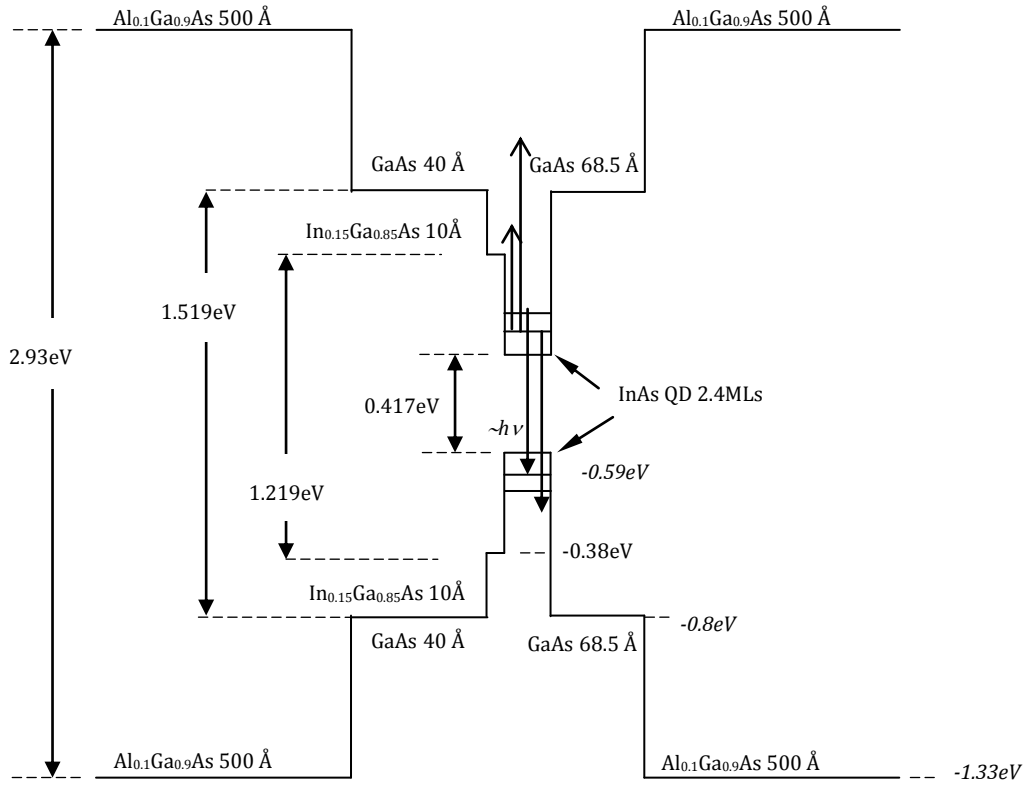


**Figure 3.12: The unstrained energy band structure.**

Figure 3.11 shows schematic of the DWELL structure and the energy band profile for the sample structure is illustrated in Figure 3.12. The valence band

offset (VBO) of the $Al_{0.1}Ga_{0.9}As$, GaAs, $In_{0.15}Ga_{0.8}As$ and InAs is -1.33eV, -0.8eV, -0.38eV and -0.59eV respectively.

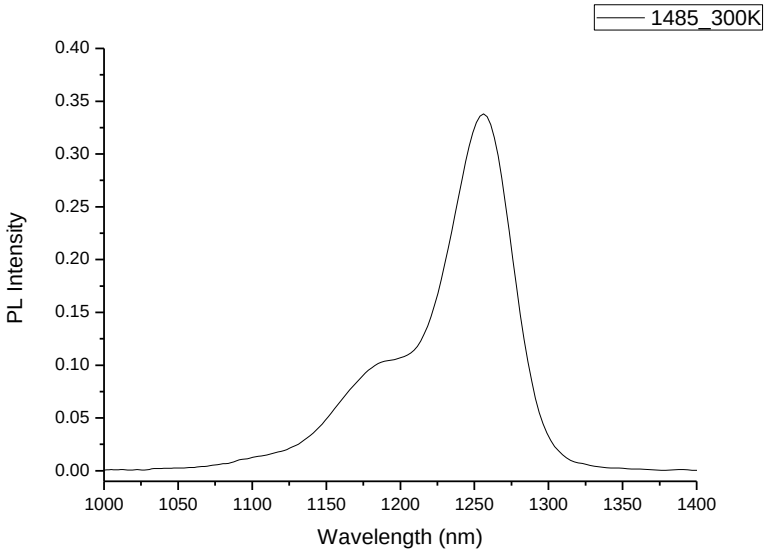


**Figure 3.13: Room temperature PL for the 30-period this InAs/ $In_{0.15}Ga_{0.8}As$/GaAs**

The room temperature PL spectrum obtained from this InAs/ $In_{0.15}Ga_{0.8}As$/GaAs dots-in-well infrared photodetector QDIP is shown in Figure 3.13. The PL wavelength of the InAs is 1255nm showing that this device is crucial to achieve quantum efficiency without introducing dislocations.

Infrared photodetectors with an InAs/ $In_{0.15}Ga_{0.8}As$/GaAs DWELL active region suffer from strain related issues. Due to high compressive strain, a greater number of active region layers cannot be grown without introducing dislocations. More layers will enhance the absorption, which in turn increases the quantum efficiency,$\eta$ of the photodetector. This increase in $\eta$ will increase the responsivity and detectivity of the detectors.

In order to determine the energy levels it is necessary to include the effects due to strain on the structure. The energy values of the QW's are affected by the strain in the layers (Osbourn, 1982). GaAs has a direct energy gap at the $\Gamma$ point of 1.519 and InAs has a direct energy gap of 0.417 at the $\Gamma$ point. Thus the value of $In_{0.15}Ga_{0.8}As$ is less of GaAs and has been obtained from the ternary

calculation depending on the alloy composition using a simple quadratic equation;

$$E_g(A_{1-x}\,B_x) = (1-x)E_g(A) + xE_g(B) + x(1-x)C \qquad (3.1)$$

where C is the bowing parameters that has been obtained from linear interpolation between the two A and B binaries (Vurgaftman & Meyer, 2001).

The lattice mismatch between the substrate, the QWs and the other material in the sample is not too large, so when the mismatch is less than 7%, it is assumed that no misfits are generated at the interfaces by compression or expansion of the planes (Osbourn, 1982) and (Vurgaftman & Meyer, 2001). This means that the strain in the materials consist of uniform biaxial strain (hydrostatic) parallel to the interface and unaxial strain parallel to the growth direction. The hydrostatic component of compressive strain increases the bandgap and tensile strain reduces the bandgap. The strain effects not only on the band edges but also modifies the effective massed associated with the individual bands. The strained-induced of the bulk material responds to the shift of energies in QWs and barrier heights. The hydrostatic strain is obtained using below equation;

$$\varepsilon_{\parallel} = \varepsilon_{xx} = \varepsilon_{yy} = \frac{a_s - a_e}{a_e} \qquad (3.2)$$

$$\varepsilon_{zz} = -2\frac{C_{12}}{C_{11}} \qquad (3.3)$$

where $\varepsilon_{xx}$, $\varepsilon_{yy}$ and $\varepsilon_{zz}$ are diagonal strain components of strain tensor is defined to be negative for compressive strain. $a_s$, is the lattice constant for the substrate and $a_e$, is the epilayer lattice constant. $C_{12}$ and $C_{11}$ is the elastic constants. The material parameters for the calculation of bandgap, VBO and strain are taken from Vurgaftman & Meyer (2001).

Energy bandgap change in the conduction band, $\Delta E_c$ and valence band, $\Delta E_v$ is given by;

$$\Delta E_c = a_c(\varepsilon_{xx} + \varepsilon_{yy} + \varepsilon_{zz}) \qquad (3.4)$$

$$\Delta E_v = a_v(\varepsilon_{xx} + \varepsilon_{yy} + \varepsilon_{zz}) \tag{3.5}$$

From the Bir-Pikus strain interaction it is not sufficient to describe the full effect of the valence band strain. Shear deformation potential, $b$ is necessary to explain the shear deformation that split the valence band into heavy/light hole. The + and – signs refer to heavy and light hole respectively.

In order to calculate the $\Delta E_c$ and $\Delta E_v$ for the ternary materials linear interpolation between the binary data obtain from Vurgaftman & Meyer (2001) is used to determine the values if the parameters used.

It has been calculated that very small lattice constant difference between the substrate and the epilayer materials, very small strain value to the energy gap produced by the calculation. The QWs calculation was performed using formulas obtained from (Pryor & Pistol, 2005) and (Micaleff & Wiess, 1990) by PhD student in the group. The QDs strain can only be obtained using numerical calculation therefore, in this study values are obtained from numerical calculation using finite element method by PhD student in the group. Figure 3.14 shows the strained conduction band profile produced numerically.

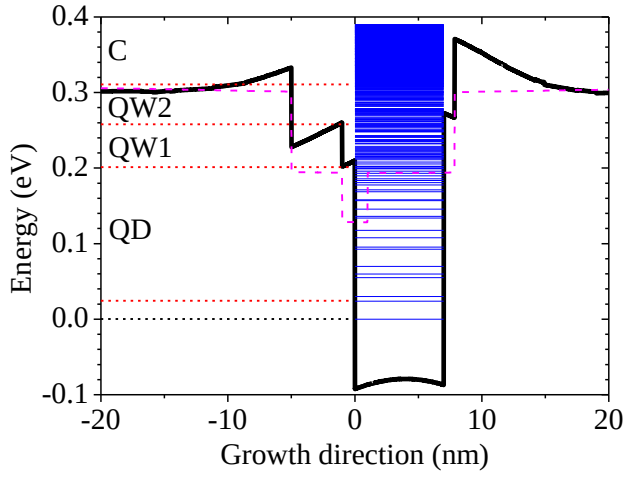


**Figure 3.14: The strained conduction band for InAs/ $In_{0.15}Ga_{0.8}As$/GaAs DWELL through the centre of the QD (solid line) and through the QW without crossing the dots (dashed line).**

## 3.5 Experimental Study

The aim of this project is to study the optical properties of the DWELL QDIP sample using experimental techniques. The experimental work on this project focuses studying the optical properties by the means of photoluminescence and photocurrent.

### *Photoluminescence (PL) Measurement*

Photoluminescence (PL) is the spontaneous emission of light from a material's optical excitation used to investigate the optical properties of the samples. PL investigations can be used to characterize both intrinsic electronic transitions and electronic transitions at impurities as well as defects in semiconductors and insulators. PL is the typical technique used for characterization of III-IV semiconductors due to the advantage of non-destructive, non electrical contact which requires minimal effort for sample preparation. PL detects the optical transition from an excited electronic state to lower electronic states, usually the ground states (Figure 3.15). Only transitions from the lower electronic states can generally be observed at low temperatures because of rapid thermalisation. Most of the light results from the difference in energy of the excited electron returning to its ground state.

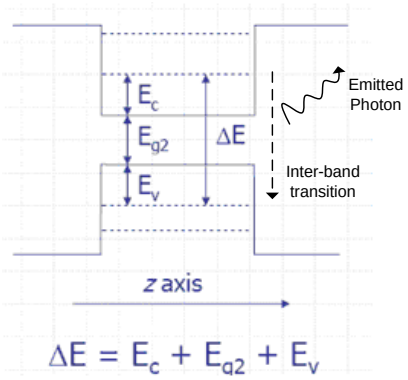


**Figure 3.15: Photoluminescence mechanism and relationship with electronic band structure**

The PL spectra have narrow band which makes the analysis possible (Strading & Klipstein, 1990). The position of PL peaks is related to the energy of each

excited level and can be used as sensitive probe to find impurities and other defects in semiconductors. The PL intensity can give more information on the quality of interfaces and surfaces. PL spectrum and the dependencies on its intensity on the irradiation intensity and device temperature provide important information for device characterisation. PL spectra and the intensity can be used determine the energy gap or wavelength of maximum gain, understand the component of ternary/quaternary layers its impurity levels and allows for the understanding and investigations of the recombination mechanism investigations (Gfroerer, 2000)

The PL measurement were completed using a Fourier Transform Infrared (FTIR) spectroscopy, FTIR is an efficient and dynamic technique that provides qualitative and quantitative information which require a broadband range from Near-IR to Far-IR spectrum. FTIR spectrometer collects and examines all wavelengths simultaneously instead of viewing each one separately. This technique is known as Felgett or multiplex advantage. The interferometer will produce infrared spectra by collecting the interferogram of a sample that involves Fourier Transform mathematical manipulation that can involve phase correction and apodization. The basic spectrometer components in the FTIR system are the detector, interferometer and radiation source as illustrated in Figure 3.16. The simple illustration of basic FTIR spectrometer for the purpose of absorption, reflectance and transmission measurement is shown in Figure 3.16.

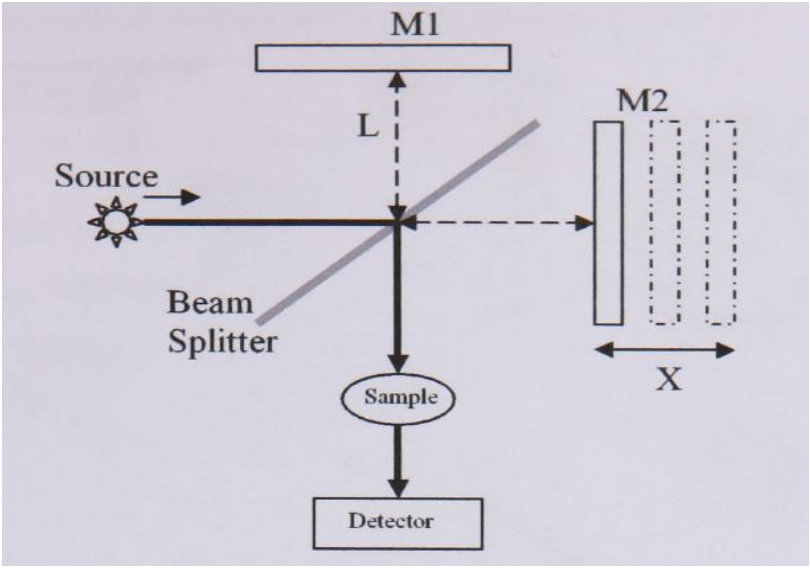


**Figure 3.16: The basic optical layout of FTIR spectrometer for absorption, transmission and reflectance measurements.**

***PL Experimental Setup and Procedures***

Photoluminescence measurement was carried out using FTIR spectrometer, where the setup was aligned with the sample as shown Figure 3.17.

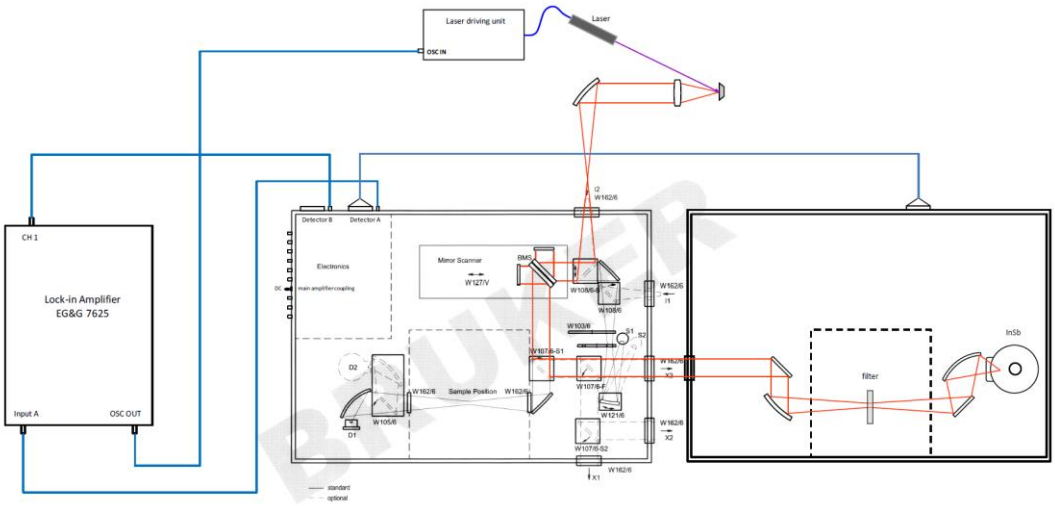


**Figure 3.17: FTIR PL measurement setup.**

From the diagram it is shown how the beam movement from the sample through the beam splitter, going through the filter in the external compartment and to be detected by the InSb detector. A GaAs semi-insulating substrate used

to filter out any emission below 1μm. From the diagram it can be elaborated that the equipments that has been used for the PL measurement are Bruker IFS/66S model with A172 external compartment, Oxford Instrument OptistatDN Cryostat, Liquid nitrogen cooled InSb detector, EG&G Instruments 7265 DSP Lock-in Amplifier, KBr beam splitter, Edwards pumping system, Penning B pressure controller, Oxford Intelligent ITC temperature controller and a PC with OPUS software.

In order to obtain the PL spectra these steps has been taken as experimental setup (Figure 3.18). The sample wafer was bonded to a holder which was inserted onto a sample rod. This was then lowered into the Oxford Instruments cryostat and all locked into place using the instrument clamps. The cryostat was capable of liquid nitrogen $LN_2$ cooling, a facility that was employed with most measurements (Figure 3.19). To do this, the cryostat was evacuated first using a rotational vacuum pump, followed by a high performance turbo pump as shown in Figure 3.20, until pressures in the cryostat reached high vacuum conditions (in the $10^{-6}$ Torr range). Liquid nitrogen was then poured down a funnel into the InSb detector jacket to cool it down to operating temperature (77K). The cryostat heat exchanger was filled with helium gas and then a funnel used to release about a litre of liquid nitrogen into the cryostat's $LN_2$ storage chamber. The desired sample temperature was digitally selected using the ITC temperature controller. The temperature control is either lowering temperature by introducing $LN_2$ into the heat exchanger surrounding the sample or increased temperature using a heater built into the cryostat, all of which is electronically managed by the temperature controller.

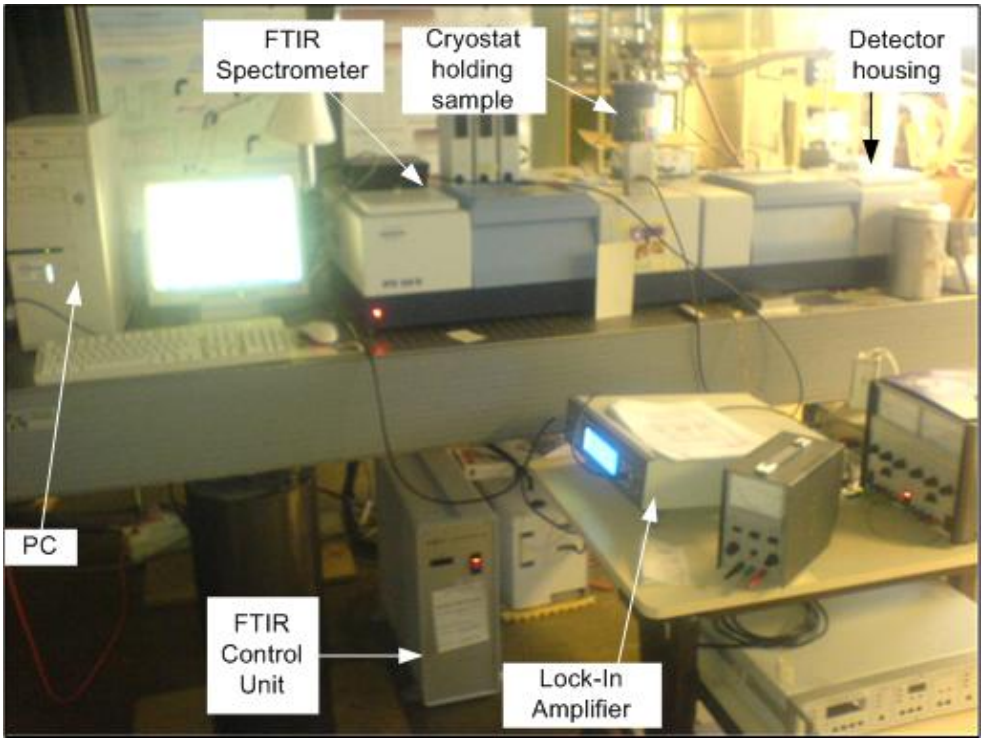


**Figure 3.18: The experimental layout in the lab showing the important equipments.**

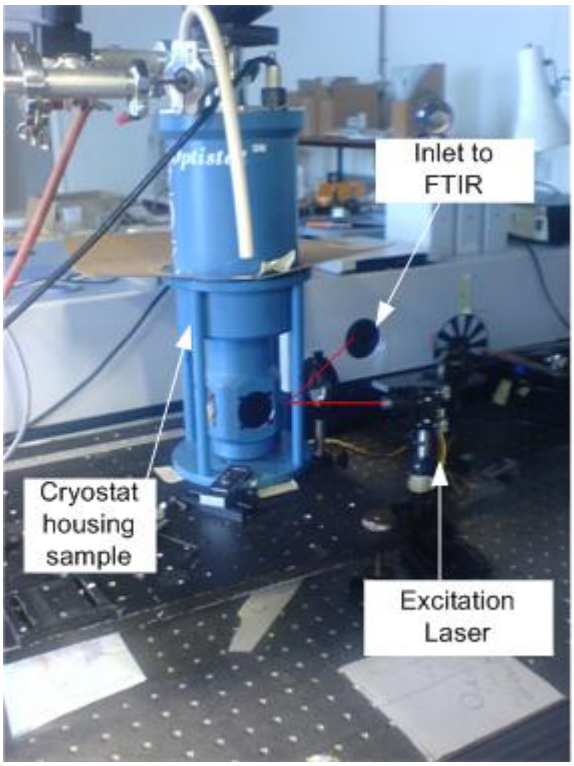


**Figure 3.19: The cryostat and the laser source.**

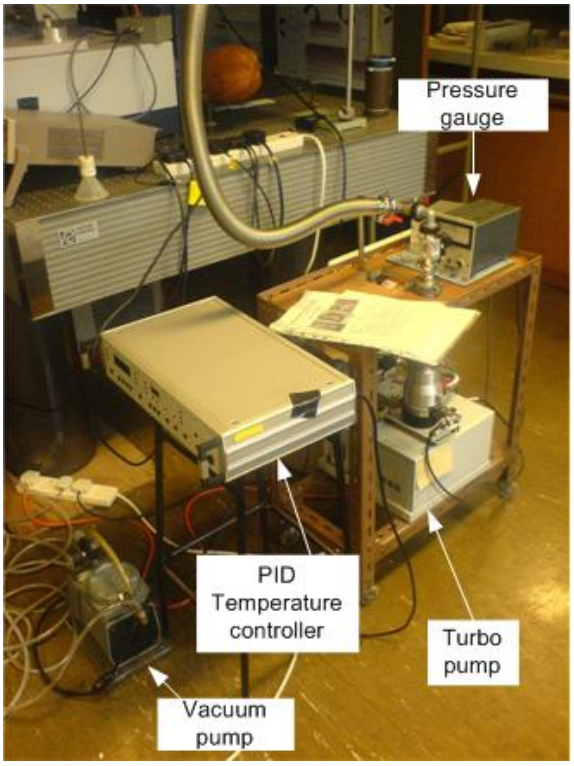


**Figure 3.20: The rotational, turbo pump and temperature controller.**

The Lock-in Amplifier (LIA) was used to modulate the laser beam to 999Hz using the laser's modulation input. The FTIR was then initialised and desired hardware parameters set using the OPUS PC application. OPUS was then used to initiate the FTIR scan and format the output data as required.

### *Photocurrent (PC) Measurement*

In contrast to other absorption-like spectroscopy, photocurrent (PC) is a comparatively simple, fast and easy to acquired technique, which reveals clear and unambiguous excitonic absorptions of self-assembled QDs. In the PC spectroscopy, the undergone processes of the photogenerated carriers are complementary to the PL measurements. The simplified photocurrent setup is shown below.

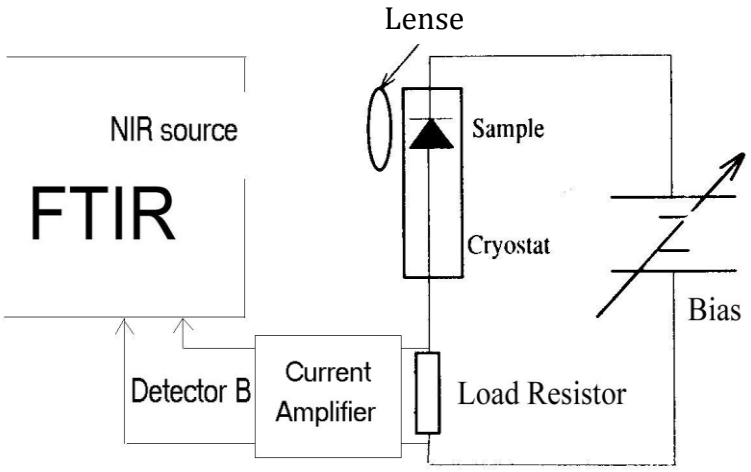


**3.21: Photocurrent measurement setup using a current pre-amplifier and Fourier Transform Infrared Spectroscopy**

The measurement has been taken using rapid scan due to some problems with the setup and lab condition, which is time constrain. The best approach would be using step scan for better spectra. Rapid scan seep mirror quickly by averaging many interferograms, it is a fast mesurement technique. The resolution of the spectra is low and not suitable for low signal with high background noise. The resolution of a measurement is simply given by how far in pathlength difference, *x* to measure. A step-scan measurement is step to step measurement for each *x* position. It is a recommended type of measurement for low signal in order to get fast time resolution however a few initial runs need to be performed to obtain a stable condition for this measurement (Berthomieu & Hienerwadel, 2009).

# Chapter 4 Results and Discussion

## 4.1 Introduction

The aim of this project is to study the optical properties of the QDIP samples using experimental techniques by means of photoluminescence spectroscopy and photocurrent measurement. In this study both temperature and power dependent measurements were performed. This section will summarize the results and discuss the main findings.

## 4.2 Photoluminescence Results

### *4.2.1 Temperature Dependence*

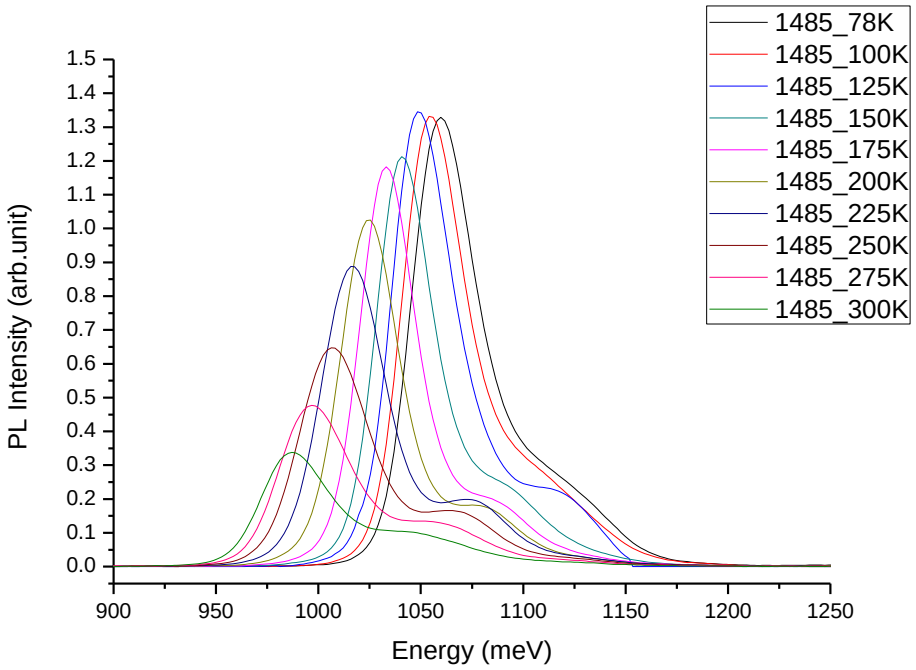


**Figure 4.1: PL spectra for sample VN1485 at temperatures from 78K to 300K**

*Sample VN1485*

The spectra show a main peak, with a higher energy (ground state) lower intensity (excited state) shoulder. As temperature is reduced, the spectrum shifts towards the red which is to higher wavelengths. As to the variation of

peak emission intensity with temperature, it appears that the peak intensity increases slightly as temperature is increased from 78K, peaking at 125K, before reducing substantially towards 300K.

For purposes of clarity, the spectra in Figure 4.1 were all normalized and plotted in Figure 4.2. It is clear that the spectral main peak red-shifted with reducing of temperature, where at 78K the ground state peak is at 2.24μm and reducing to 1.9μm at 300K. The higher energy shoulder is visible in each spectrum as well.

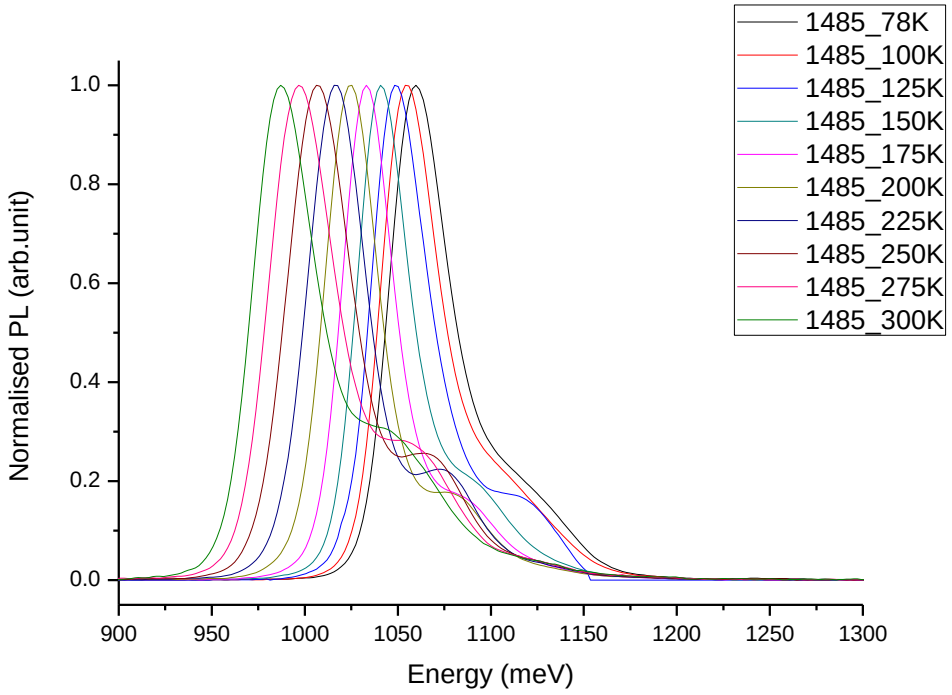


**Figure 4.2: Normalised PL spectra for sample VN1485 at temperatures from 78K to 300K**

To aid in the analysis, the data was fitted to two Gaussian curves (e.g. Figure 4.3, at 225K), the sum of which would account for a main peak and shoulder. The curve fitting tool in OriginLab was applied to the spectral data, with fits made to using fit linear curve. The integrated intensity was then obtained by numerical integration of the Gaussian curves.

At 78K the PL transition energy is found to be 1.14eV from the experimental result, and comparing to the modelling calculation provided by the optoelectronics research group it is assumed that the Ga content, x in the InAs dot is between 30%. The modelling result is based on undoped material only therefore no comparison can be made for the doped sample.

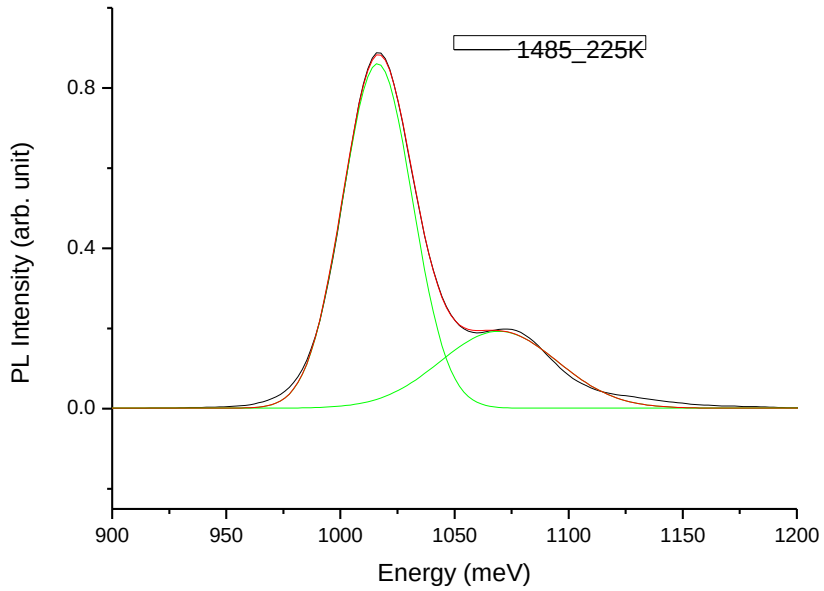


**Figure 4.3: Example of curve fitting to two Gaussians at 225K**

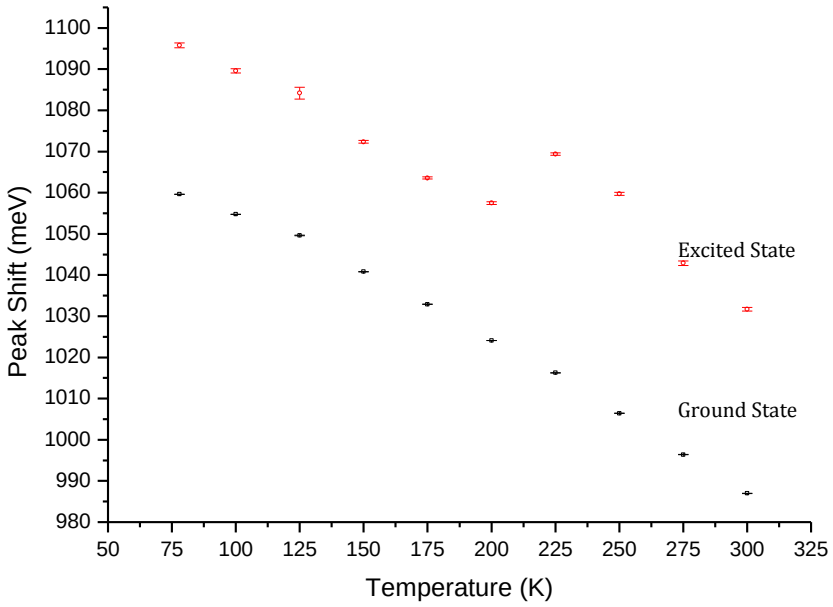


**Figure 4.4: Variation of peak shifts with temperature from 77K to 300K**

The above figure shows peak shifts values obtained after fitting the spectra to two Gaussian peaks. There is a consistent red-shift with increasing temperature in the ground state. This effect commonly referred to as lattice dilation is consistent with theory. At low temperature the ground state peak is at 1.06eV reducing to 0.98eV at the room temperature showing 72meV in difference. For the excited state peak shift can be observed steady reduce of energy until 225K and 250K where the energy increased before reducing steadily up to 300K. This needs further investigation via more experimental measurements to verify this behaviour.

As temperature increases, the inter-atomic spacing increases, leading to a reduced potential experienced by charge carriers in the lattice. In order to maintain the consistency between the theoretical and experimental results for the temperature dependence, the results has been compared with empirical calculation using Varshni equation;

$$E_g(T) = E_g(T=0) - \frac{\alpha T^2}{T+\beta} \tag{4.1}$$

Where α and β are the adjustable Varshni's parameter. Conforming to the calculation the result shows that the energy gap for III-IV semiconductor decreases with increasing of semiconductor.

*Sample VN1486*

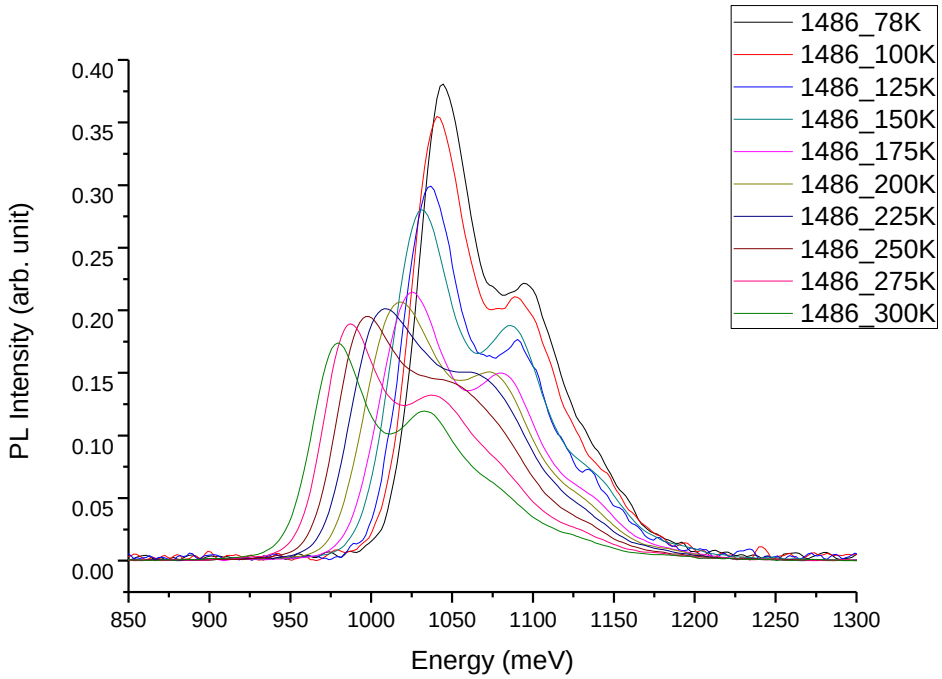


**Figure 4.5: PL spectra for sample VN1485 at temperatures from 78K to 300K**

The PL measurement in Figure 4.5 is performed under same excitation power for this sample. At 78K the ground state peak is at 2.18μm reducing to 1.96μm at 300K. This sample has been doped in the GaAs QWs layer at 1 electron per dot. For PL transition this sample did not show significant different in the PL intensity compared to the undoped sample. The excited state energy level shows some different where the values increased and more significant of the second shoulder can be observed as shown in the normalised PL spectra (Figure 4.6). This could be due to transition between the lowest energy states in the conduction band to the higher energy states in the valence band.

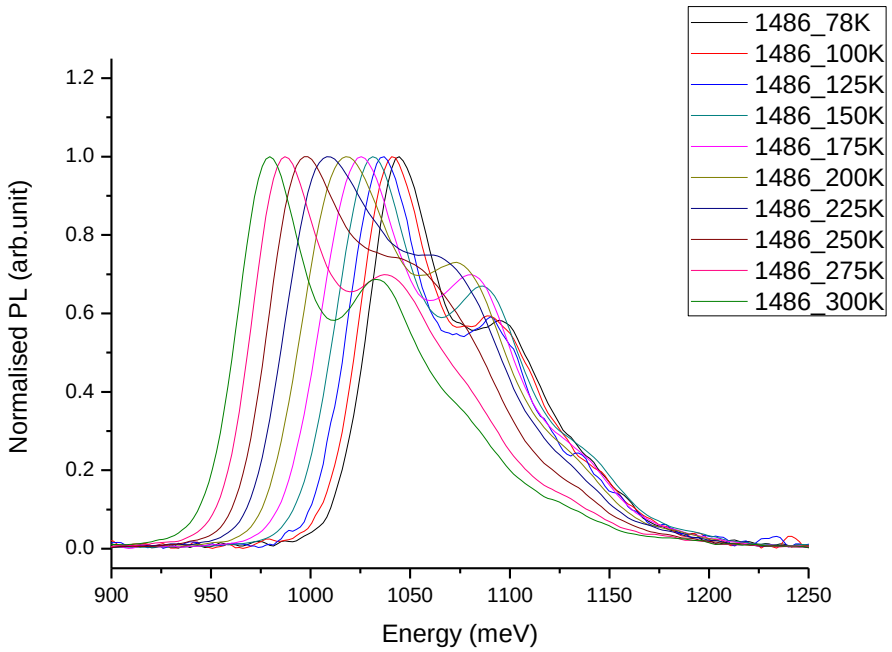


**Figure 4.6: Normalised PL spectra for sample VN1485 at temperatures from 78K to 300K**

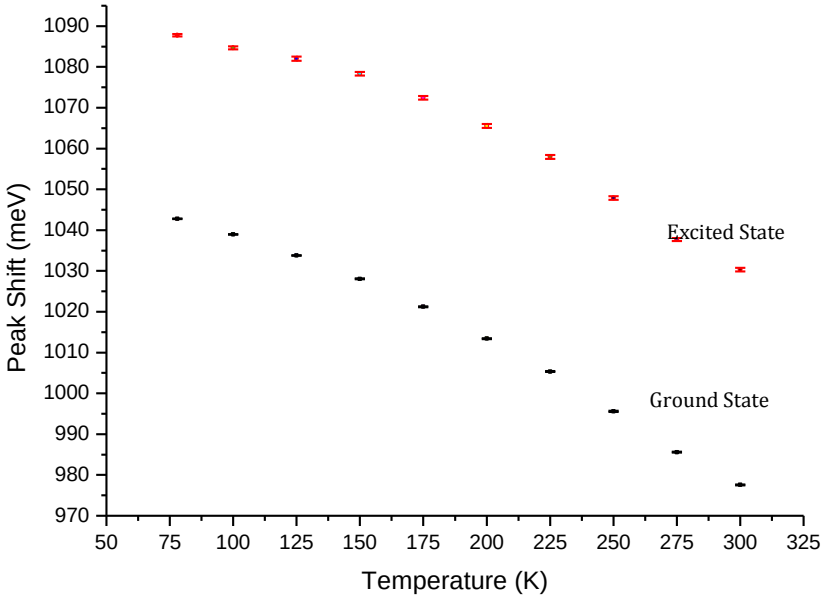


**Figure 4.7: Variation of peak shifts with temperature from 77K to 300K**

Lookin at Figure 4.7, the PL shift is reducing consistently for ground state and excited states can be observed in the peak shift. Unlike the first sample (VN1485) the peak shifts in the excited state not responding stably to the rising temperature. At low temperature the peak value is 1.09eV reducing to 1.3ev at room temperature giving ~58meV in different.

### *4.2.3 Power Dependence*

PL measurements were therefore taken at 250K, 150K and 78K with the laser power varying from the default 5mW down to 40mW. Due to the low PL intensities at low excitation power, it was necessary to take longer scans at 5mW compared to 40mW, in a bid to improve the SNR. The resulting spectra are illustrated in Figure 4.8. The peak energy of the samples shifted to higher energy as the excitation power increased from 5mW to 40mW. The energy peak reduced as the temperature increases for both samples. For sample VN1486 (Figure 4.9), more significant peak energy reduce can be observed up to ~0.5eV difference at low temperature. The energy difference for this doped sample gets smaller as the temperature increase to 250K.

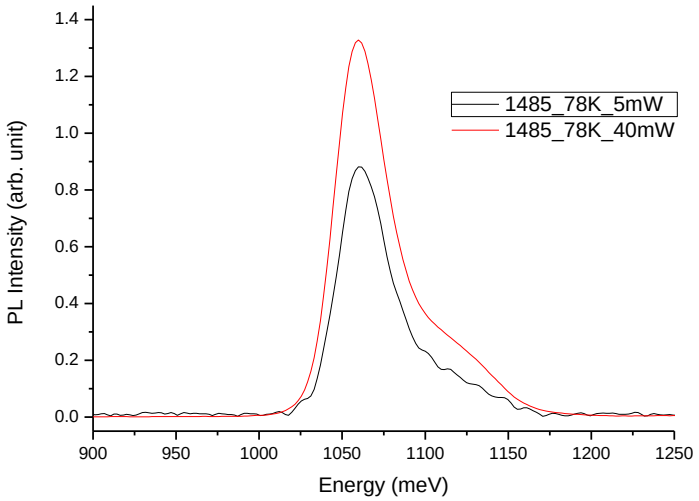


(a)

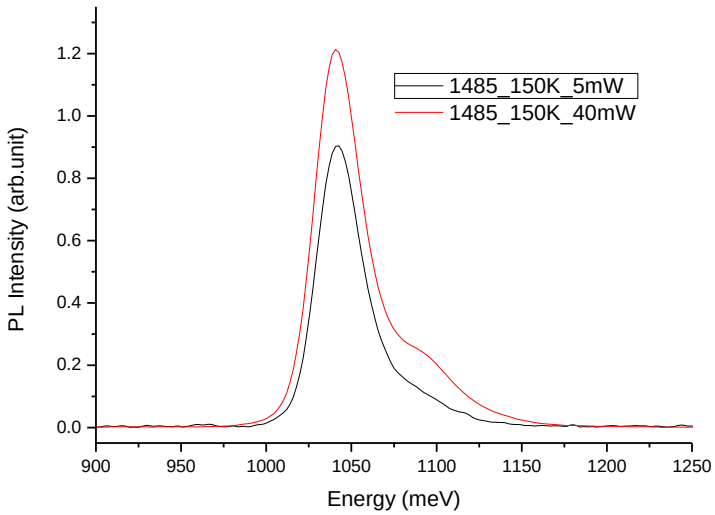


(b)

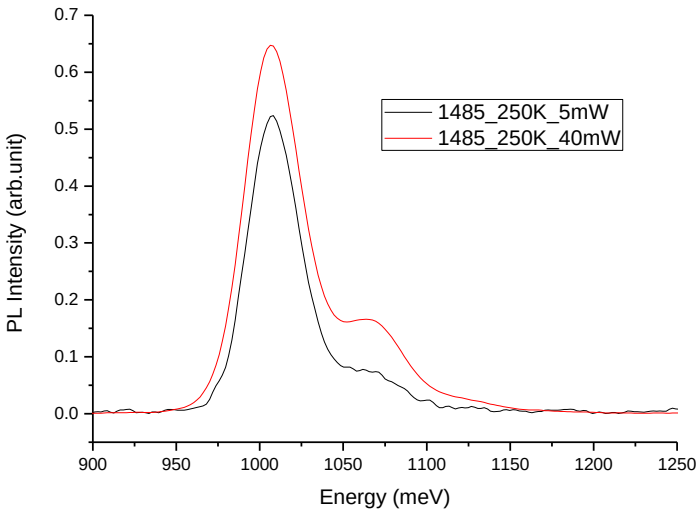


(c)

**Figure 4.8: PL spectra for VN1485 power dependence (a) at 78K, (b) at 150K and (c) at 300K**

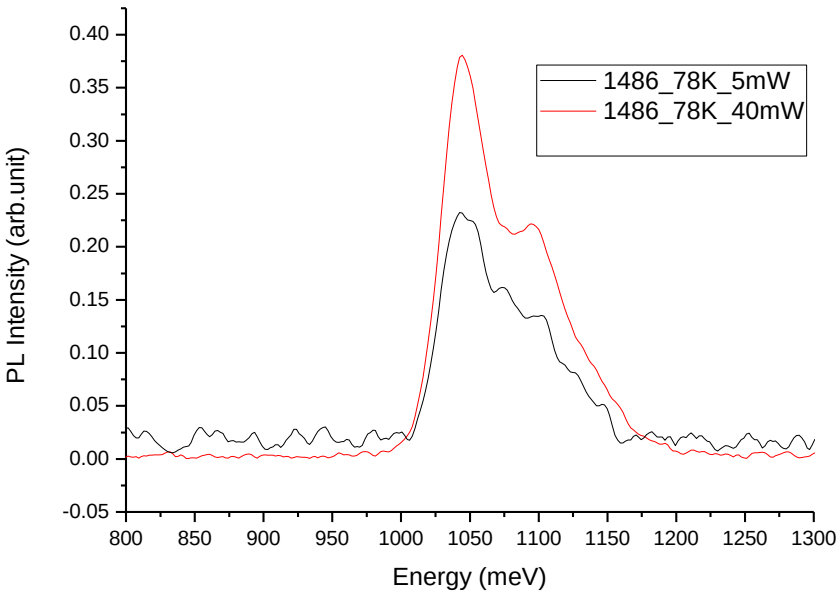
1486_78K_5mW
1486_78K_40mW
PL Intensity (arb.unit)
Energy (meV)
0.40
0.35
0.30
0.25
0.20
0.15
0.10
0.05
0.00
-0.05
800
850
900
950
1000
1050
1100
1150
1200
1250
1300

(a)

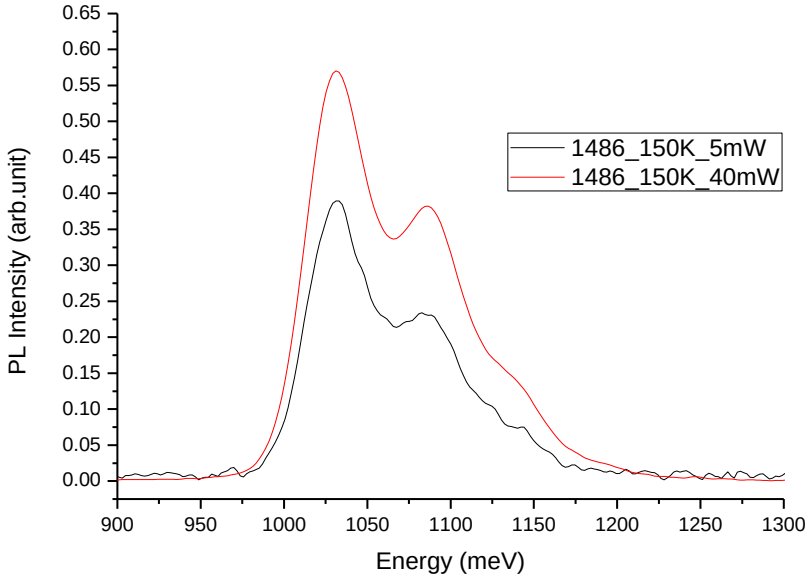
1486_150K_5mW
1486_150K_40mW
PL Intensity (arb.unit)
Energy (meV)
0.65
0.60
0.55
0.50
0.45
0.40
0.35
0.30
0.25
0.20
0.15
0.10
0.05
0.00
900
950
1000
1050
1100
1150
1200
1250
1300

(b)

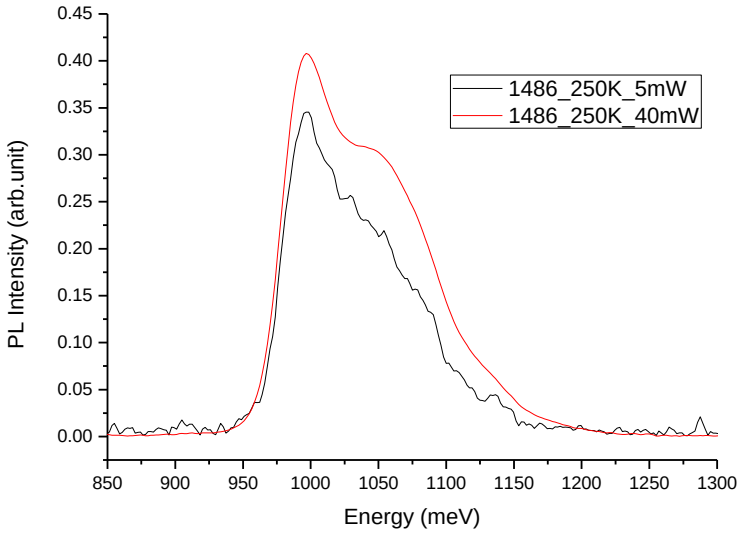


(c)

**Figure 4.9: PL spectra for VN1486 power dependence (a) at 78K, (b) at 150K and (c) at 300K**

## 4.3 Photocurrent Results

Infrared detectors based on DWELL design primarily work on bound-to-bound transitions from the ground electronic state of the InAs QD to the $In_{0.15}Ga_{0.85}As$ QW and bound-to-continuum transition from the ground electronic state of the InAs QD to a state in the GaAs barrier depending on the applied bias, one of the transitions is observed in the spectral response for the detector. The undoped sample do not show much response up to 10V of applied bias, therefore only photocurrent spectra for the doped sample (VN1486) was obtained from the experimental result. The transition is not observed at zero bias low probability of carriers tunnelling from QW state.

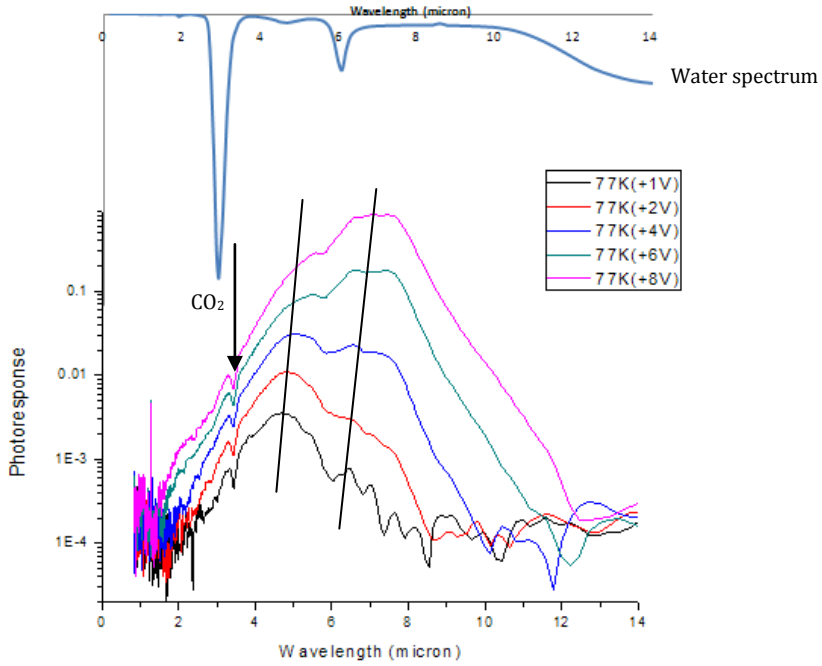


**Figure 4.10: Photoresponse of VN1486 at 77k for different applied positive voltages**

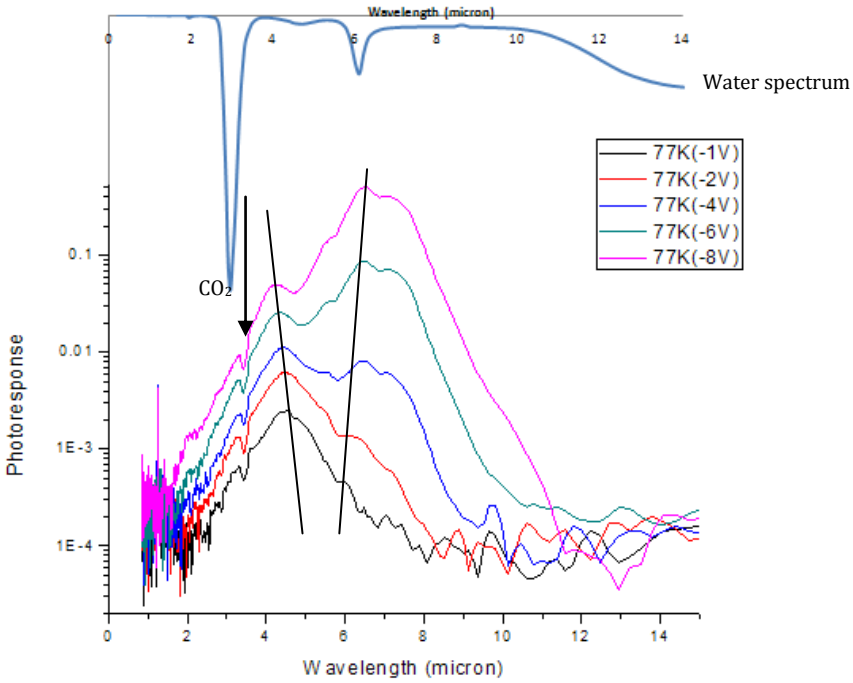


**Figure 4.11 The photoresponse of VN1486 at 77K for different applied negative bias.**

The spectral response of the detector shows two important peaks. The distortion in the spectral response is due to atmospheric (water and $CO_2$) absorption. At positive bias in Figure 4.10, the peak is located at about 225meV corresponding to a wavelength of 4.5μm -5.5μm. This peak results from electrons excited from the ground state in the QDs to higher energy states in the QW which then tunnel through the quantum well barrier and shown in Figure 4.12.

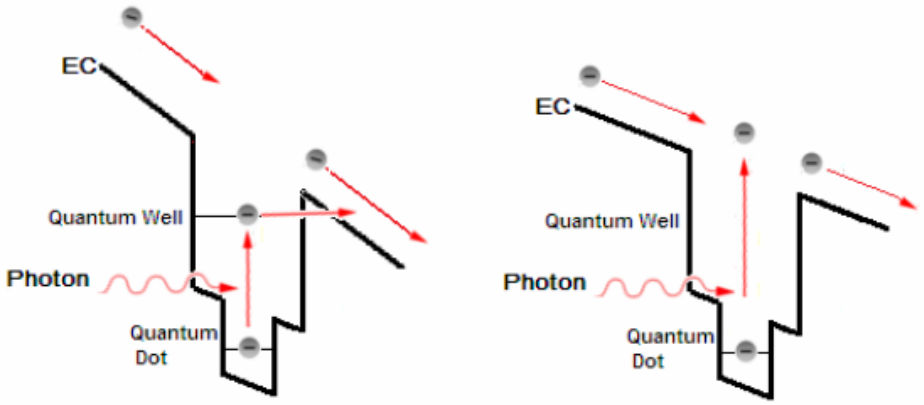


(a) (b)

**Figure 4.12: The two main important photocurrent peaks graphical explanation, (a) responding to the tunnelling effect, (b) transition from ground state to the conduction band.**

When the bias is decreased, the effective tunnel barrier becomes wider and the tunnel probability for electrons becomes smaller. If the applied bias is increased the quantum wells are tilted further which results in thinner tunnelling barriers and more electrons can now tunnel through the quantum well barrier. The second peak in Figure 4.10 is located at about 165meV and corresponds to a wavelength from 6.5μm -7.5μm. This peak is created by electrons excited from the ground state in the quantum dots to the matrix. Figure 4.11 shows the photoresponse of the same sample at 77K for different negative bias. The spectral response of the negative bias has almost same shape with the negative bias. The difference between the samples is just the fact that for the negative bias the first peak is located at around 300mev corresponding to a wavelength from 4.2μm -4.3μm. The second peak is located at about 190mev corresponding to wavelength from 6.0μm – 6.4μm.

**Bias range +2V to +8V**

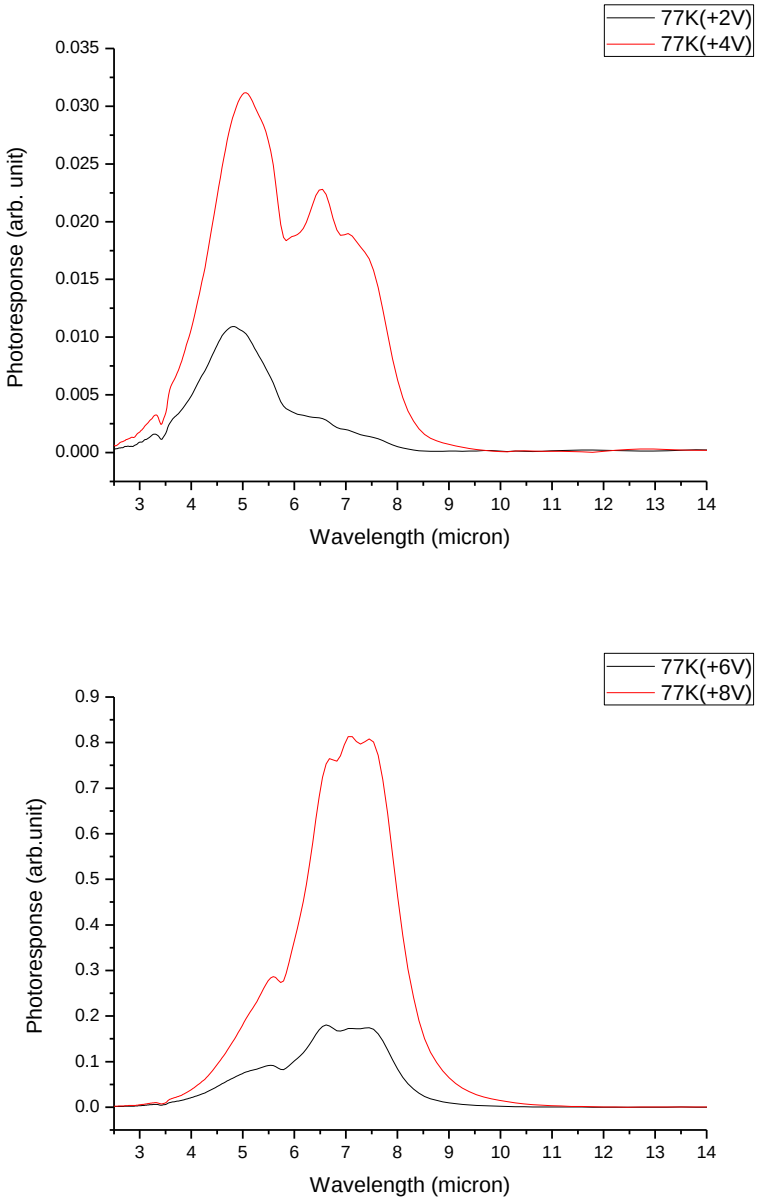


**Figure 4.13: Spectral response taken at 77K for bias range (a) 2V-4V and (b) 6V-8V.**

Referring to Figure 4.13(a) from 2V to 4V, the peak response is at 5.05μm for first peak and at 6.5μm for the second peak. From 6V to 8V 6.5μm is the dominant peak response and weaker response on the second peak. This 6.5μm (~191meV) is suspected to be bound-to-bound transition from the ground state in InAs QD to GaAs QW in the device.

**Bias range -2V to -8V**

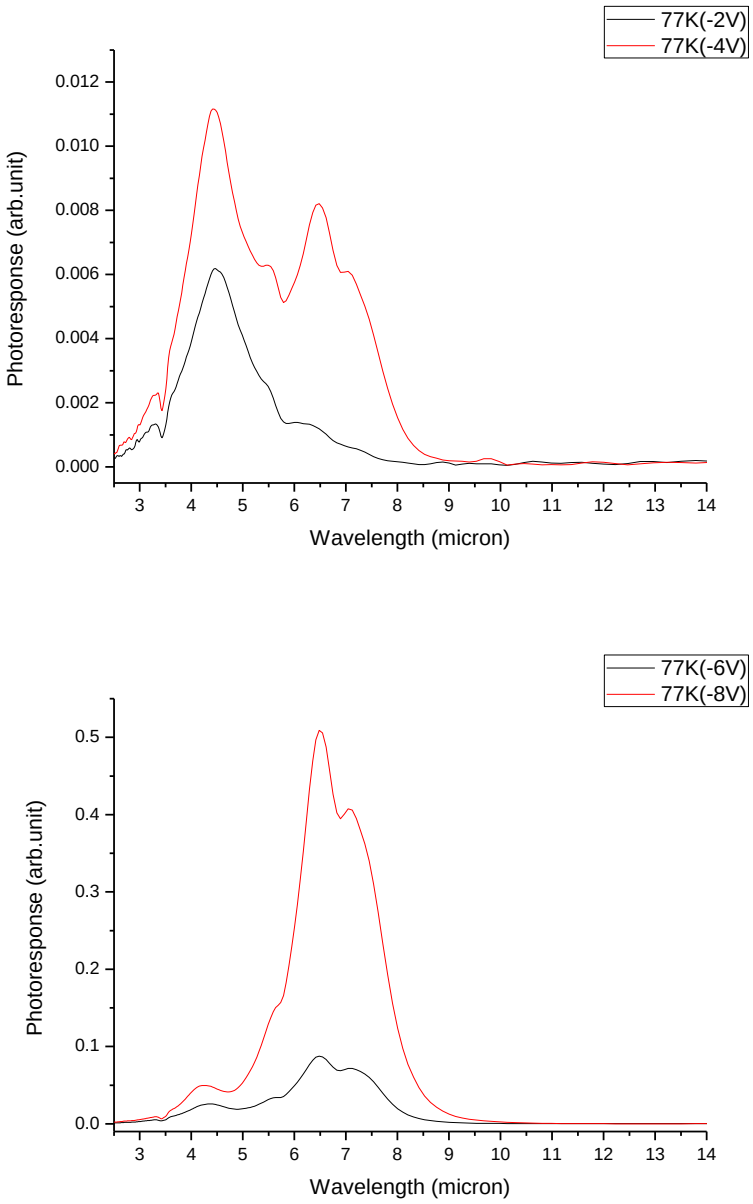


**Figure 4.14: Spectral response taken at 77K for bias range (a) -2V to -4V and (b) -6V to -8V.**

In Figure 4.14 the bias range from -2V to -8V the peak response at the range from 4.5μm to 7.2μm. The peak response at bias range -2V and -4V is at 4.4μm for the first peak and around 6.5μm at the second peak corresponding to ~280meV. The peak response at bias range -4V to -8V is at 6.5μm for the first peak and around 7.16μm at the second peak. This bias tunable response has

been observed in the standard DWELL detectors and reported in many studies. This effect is believed to be the quantum confined stark effect (QCSE) exploited by the asymmetry effect in the bandstructure (Shenoi, et al., 2008).

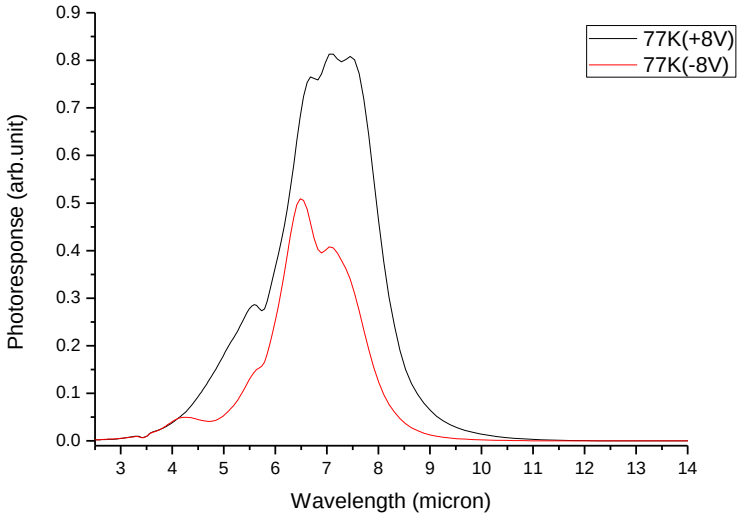


**Figure 4.15: Spectral response taken at 77K for +8V and -8V.**

In Figure 4.15 the photocurrent spectrum at +8V is red-shifted with respect to that at -8V, indicating an asymmetric dependence on applied bias due to off-centre position of the QDs layer in the well. This tuning effect responds to different tilting directions of the energy band when the polarity of the bias is changed, which is the energy separation between the QD states and the QW states depends on the tilting direction (Figure 4.16).

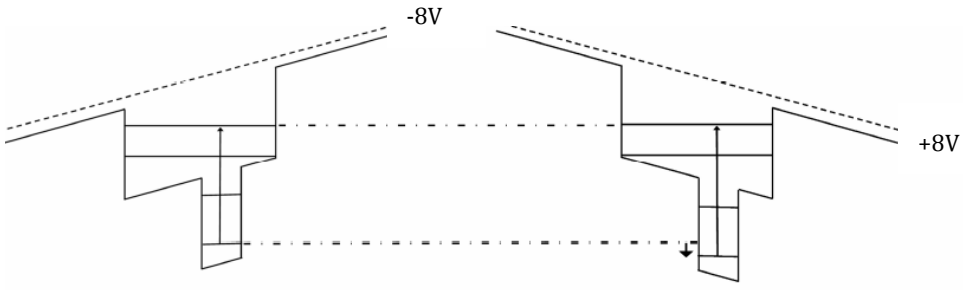


**Figure 4.16: Tuning of the wavelength by reversing the applied bias at a temperature of 77K.**

# Chapter 5 Conclusion

This study has presented the mid-wavelength infrared QDIP with 30-layers of DWELLs in the active region where special attention has been given to the optical properties of the intersubband photodetector namely the DWELL detector. The photoluminescence and photocurrent of the device has been investigated.

The results have demonstrated impressive outcome which is good control over the operating wavelength, higher operating temperature and bias tunable spectral. The photoresponse of the DWELL showed a dependence on the applied bias due to the tilting of the conduction band edge and the change in probability of tunnelling from the quantum well excited states through the barriers. By changing the bias it is possible to tune the wavelength window of the detector.

Due to time constraint, the photocurrent measurement was done in rapid scan mode. Therefore future work might provide useful information if using step-scan mode and purging the air with nitrogen gaseous for better spectral. In future it is possible to engineer the sample for mid-infrared, far-infrared and terhertz frequencies in order to optimise the performance.

# References

A.Y.Cho. (1971). Film Deposition by Molecular Beam Techniques. *Journal of Vaccum Science Technology* (8), 31-38.

A.Y.Cho. (1979). Recent Developments in structures Molecular Beam Epitaxy (MBE). *Journal of Science Technology , 16*, 275-284.

Broekart, T. P., & Fonstad, C. (1992). Novel Organic Acid Based Etchants for InGaAlAs/InP Heterostructure Devices with AlAs Etch-Stop Layers. *Journal of Electrochemical Society , 139* (8).

Chang, L., L.Esaki, Howard, W., R.Ludeke, & G.Schul. (1973). Structures Grown by Molecular Beam Epitaxy. *Journal of Vacuum Science Technology* (10), 655-662.

Colorado, U. o. (2010). *IR Spectroscopy Tutorial.* Retrieved August 25, 2010, from Spectroscopy: http://orgchem.colorado.edu/hndbksupport/irtutor/main.html

Gupta, R., Lai, K. T., Missous, M., & Haywood, S. K. (2004). Subband nonparabolicity estimated from multiple intersubband absorption in highly doped multiple quantum wells. *Physical Review B , 69* (3), 033303.

Gupta, R., Wong, A. L., & Haywood, S. K. (1999). 3μm intersubband Quantum Well Photodetector (QWIP). *Tr. Journal of Physics , 23*, 673-679.

Haywood, S. K., Lai, K. T., & Missous, M. (2006). *Mid-infrared Semiconductor Optoelectronics.* Berlin: Springer.

Krishna, S. (2005). Quantum dots-in-a-well infrared photodetectors. *Journal of Physics D: Applied Physics , 38* (13), 2142-2150.

Levine, B. F. (1993). Quantum-well infrared photodetectots. *Journal of Applied Physics , 74* (8), 1-81.

Ling, H. S., Wang, S. Y., Lee, C. P., & Lo, M. C. (2008). High quantum effieciency dots-in-a-well quantum dot infrared photodetectors with AlGaAs confinement enhancing layer. *Applied Physics Letters , 92* (19), 193506.

Liu, H. C. (2003). Quantum dot infrared photodetector. *Opto-epectronics Review , 11*, 1-5.

Martyniuk, P., Krishna, S., & Rogalski, A. (2008). Assessment of quantum dot infrared photodetectors for high temperature operation. *Journal of Applied Physics , 104* (3), 034314.

Mashade, M. B., Ashry, M., & Nasr, A. (2003). Therotical analysis of quantum dot infrared photodetectors. *Semiconductor Science and Technology , 18* (9), 891-900.

Micaleff, J., & Wiess, B. L. (1990). The refractive index of III-Iv semiconductor strained-layer superlattices. *Optical and Quantum Electronics* , 669-684.

Osbourn, G. (1982). Journal of Applied Physics. *Strained layer superlattices from lattice mismatch materials , 53*, 1586-1589.

Parker, G. (1994). *Introductory Semiconductor Device Physics.* Prentice Hall International (UK) Limited.

Philips, J. (2002). Evaluation of the fundamental properties of quantum dot infrared detectors. *Journal of Applied Physics , 91* (7), 4590-4594.

Pryor, C., & Pistol, M. (2005). Bande-edge diagrams for strained III-IV semiconductor quantum wells, wires and dots. *Physical Review B , 72*, 1098-1121.

Rhyzii, V. (1997). Characteristics of quantum well infrared photodetectors. *Journal of Applied Physics , 81* (9), 6442-6448.

Rinaldi, F. (2002). *Annual Report Optoelectronics Department.* University of Ulm.

Rogalski, A. (2009). Outlook on Quantum dot infrared photodetectors. *Optical Memory and Neural Networks (information Optics) , 18* (3), 234-252.

Rogalski, A. (2002). Quantum Well Infrared Photoconductors In Infrared Detection Technology. *International Journal of High Speed Electronics and Systems , 12* (3), 593-658.

Rogalski, A. (2003). Quantum well photodetectors in infrared detector technology. *Journal of Applied Physics , 93* (8), 4355-4391.

Schneider, H., & Liu, H. C. (2007). *Quantum Well Infrared Photodetectors Physics and Applications.* Heidelberg: Springer.

Shenoi, R. V., Attaluri, R. S., Siroya, A., Shao, J., Sharma, Y. D., Stinz, A., et al. (2008). Low Strain InAs/InGaAs/ quantum dots-in-a well infrared photodetector. *Journal Vaccum Science Technology , 26* (3), 1136-1139.

Strading, R. A., & Klipstein, P. C. (1990). *Growth and characterisation of semiconductors.* Bristol: J W Arrowsmith Ltd.

Sze, S. M., & Ng, K. K. (2007). *Physics Of Semiconductor Devices.* John Wiley & Sons.

Vurgaftman, I., & Meyer, J. R. (2001). Band parameters for III-IV compound semiconductor and thier alloys. *Applied physics review , 89* (11), 5818-5875.

Wilson, J., & Hawkes, J. (1998). *Optoelectronics an Introduction.* Prentice Hall.

# Appendices

The below Gantt Chart was the preliminary plan but due to some unexpected circumstances where the lab being refurbished almost all the time during this project duration, some changes has been made towards the original plan. Supporting staff was on summer vacation as well made some of the equipment not accessible therefore required some help from University of Sheffield for sample preparation in order to complete the project on time. At later of the weeks point the lab was inaccessible during office hours due to safety reasons as the builders has been working outside the lab entrance. This issue has also caused significant delays to my project. The samples that are planned to study are not in the same wavelength therefore QWIP and QDs samples are not comparable to each other, with agreement from supervisor only study for QDIP are performed.

| | WK6 | WK7 | WK8 | EASTER BREAK | | | WK9 | WK10 | WK11 | WK12 | EXAMINATION WEEK | | | WK1 | WK2 | WK3 | WK4 | WK5 | WK6 | WK7 | WK8 | WK9 | WK10 |
|---|---|---|---|---|---|---|---|---|---|---|---|---|---|---|---|---|---|---|---|---|---|---|---|
| Project Plan | | | | | | | | | | | | | | | | | | | | | | | |
| Literature Review | | | | | | | | | | | | | | | | | | | | | | | |
| QWIP PL measurement | | | | | | | | | | | | | | | | | | | | | | | |
| QWIP PC measurement | | | | | | | | | | | | | | | | | | | | | | | |
| Compare analysis result | | | | | | | | | | | | | | | | | | | | | | | |
| QDIP PL measurement | | | | | | | | | | | | | | | | | | | | | | | |
| QDIP PC measurement | | | | | | | | | | | | | | | | | | | | | | | |
| Compare QDIP with QWIP result | | | | | | | | | | | | | | | | | | | | | | | |
| DWELL PL measurement | | | | | | | | | | | | | | | | | | | | | | | |
| DWELL PC measurement | | | | | | | | | | | | | | | | | | | | | | | |
| Compare and analyse all results | | | | | | | | | | | | | | | | | | | | | | | |
| Writing up | | | | | | | | | | | | | | | | | | | | | | | |
| | | | | | | | | | | | | | | | | | | | | | | | |

Initial Gantt Chart

| | WK6 | WK7 | WK8 | EASTER BREAK | | | WK9 | WK10 | WK1 | WK2 | WK3 | WK4 | WK5 | WK6 | WK7 | WK8 | WK9 | WK10 | WK 11 | WK 12 | WK13 |
|---|---|---|---|---|---|---|---|---|---|---|---|---|---|---|---|---|---|---|---|---|---|
| Project Plan | | | | | | | | | | | | | | | | | | | | | |
| Literature Review | | | | | | | | | | | | | | | | | | | | | |
| FTIR background theory | | | | | | | | | | | | | | | | | | | | | |
| PL setup and calibration | | | | | | | | | | | | | | | | | | | | | |
| PL measurement | | | | | | | | | | | | | | | | | | | | | |
| Sample preparation for PC | | | | | | | | | | | | | | | | | | | | | |
| PC setup and callibration | | | | | | | | | | | | | | | | | | | | | |
| PC measurement | | | | | | | | | | | | | | | | | | | | | |
| Compare and analyse all results | | | | | | | | | | | | | | | | | | | | | |
| Writing up | | | | | | | | | | | | | | | | | | | | | |

The Gantt chart showing actual progress during completion of the dissertation.